International Journal of Multiphase Flow 205 (2026) 105967

Contents lists available at ScienceDirect

International Journal of Multiphase Flow

journal homepage: www.elsevier.com/locate/ijmulflow

Research Paper

Comparative study of flow-rate dependence and end effects in steady-state two-phase flow through model pore networks

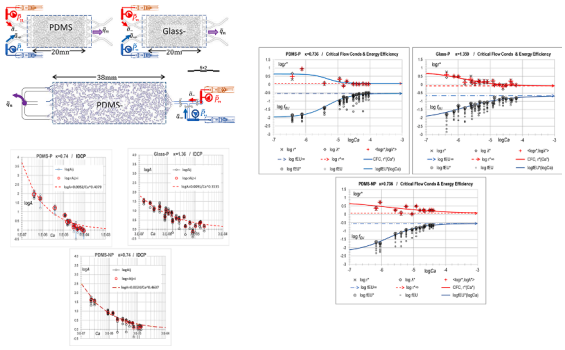
K.V. Mouravas [a,b], N.K. Karadimitriou [b], P.G. Dimitriadis [a], A.G. Yiotis [c], H. Steeb [b,d], M.S. Valavanides [a,*]

[a] Department of Civil Engineering, University of West Attica, 12241, Egaleo Attica, Greece
[b] Institute of Applied Mechanics, University of Stuttgart, 70569, Stuttgart, Germany
[c] School of Rural, Surveying & GIS Engineering, National Technical University of Athens, Greece
[d] Stuttgart Center for Simulation Science (SC SimTech), 70569 Stuttgart, Germany

HIGHLIGHTS

- Influence of pore-network geometry, wettability, and flow conditions on end effects was systematically investigated.
- Steady-state two-phase flow experiments were conducted in planar microfluidic pore networks.
- DeProF analysis quantified flow-rate-dependent relative permeability, dynamic capillary pressure, and energy efficiency.
- Sub-pore-scale imaging revealed the evolution of interstitial flow structures under transient and steady conditions.
- Macroscopic flow measurements were correlated with underlying pore-scale flow structures.

GRAPHICAL ABSTRACT



ARTICLE INFO

Keywords:
Porous media
Two-phase flow
Relative permeability
Flow-rate dependency
Intrinsic dynamic capillary pressure
SCAL
Microfluidics

ABSTRACT

This study investigates the influence of network geometry, wettability, and flow conditions on end effects during steady-state immiscible two-phase flow in model pore networks. Systematic co-injection experiments were performed in planar microfluidic networks with periodic and non-periodic geometries and varying wettability characteristics, enabling direct comparison over a broad range of flow conditions, expressed in terms of capillary number and flow-rate ratio.

Using the DeProF theoretical framework, pressure-drop measurements were analyzed to evaluate the flow-rate-dependency of relative permeabilities, intrinsic dynamic capillary pressure, and energy efficiency. In parallel, sub-pore-scale imaging provided direct insight into the spatiotemporal evolution of interstitial flow structures under both steady and transient flow conditions.

The study: (a) further validates the DeProF framework as a robust and efficient approach for analyzing two-phase flow in porous media, capturing flow-rate dependency and energy efficiency across diverse flow conditions, fluid pairs, and pore-network configurations; and (b) demonstrates its potential to infer interstitial flow-structure characteristics from ex-core (macroscopic) relative permeability measurements.

* Corresponding author.
E-mail address: marval@uniwa.gr (M.S. Valavanides).

https://doi.org/10.1016/j.ijmultiphaseflow.2026.105967
Received 16 May 2026; Received in revised form 21 September 2026; Accepted 17 October 2026
Available online 4 November 2026
0301-9322/© 2026 The Authors. Published by Elsevier Ltd. This is an open access article under the CC BY license (http://creativecommons.org/licenses/by/4.0/).
Open access publication of this article was funded by HEAL-Link under an agreement between Elsevier and HEAL-Link

Nomenclature

Subscripts, superscripts etc

~	A tilde above a letter indicates a dimensional variable; no tilde above a letter denotes a dimensionless variable
;	A semicolon separates the group of a function's arguments into independent variables and system parameters.
*	An asterisk (as superscript) indicates a value corresponding to critical flow conditions
n	index (subscript) indicating a non-wetting phase variable
w	index (subscript) indicating a wetting phase variable
i, j, k, m	indices

Physical variables – Latin letters

Ca	Capillary number
f_{EU}	energy utilization factor, or, energy efficiency
f	fractional flow
$\widetilde{k}$	absolute permeability of the porous medium
k_r	relative permeability
$\widetilde{p}$	macroscopic pressure
r	non-wetting phase /wetting-phase flow-rate ratio
S_w	wetting phase saturation
$\widetilde{q}$	flow-rate
U	superficial velocity, or, flow intensity
x	reduced macroscopic pressure gradient
$\widetilde{z}$	coordinate length along the macroscopic flow direction

Physical variables - Greek letters

$\widetilde{\gamma}_{nw}$	interfacial tension between the wetting and the non-wetting phase
θ_A	dynamic contact angle for advancing meniscus
θ_R	dynamic contact angle for receding meniscus
κ	non-wetting/wetting phase viscosity ratio
λ	non-wetting/wetting phase mobility ratio
$\widetilde{\mu}$	dynamic viscosity

Abbreviations

CEE	Capillary end effects
CFC(s)	critical flow condition(s)
IDCP	Intrinsic Dynamic Capillary Pressure
n/w	non-wetting phase / wetting phase
REV	Representative Elementary Volume
SCAL	Special Core Analysis Laboratory

1. Introduction

Two-phase flow in porous media is a fundamental process underpinning a wide range of energy and environmental applications, including enhanced oil recovery, CO_2 sequestration, geothermal energy storage, groundwater remediation, operation of trickle bed reactors and fuel cells, etc. The flow system comprises two immiscible phases flowing simultaneously through a complex network of interconnected pores. In such systems, one of the two phases, the *wetting phase*, WP, preferentially wets the solid surface against the other, *non-wetting phase*, NWP. The degree of wettability is governed by the physicochemical affinities between the two fluids and the solid matrix.

In general, the aforementioned processes span a wide range of spatial and temporal scales: pore-scale phenomena occur at micrometer to millimeter scales, while field-scale behavior extends from meters to a few hundreds of meters, Fig. 1. Correspondingly, the governing

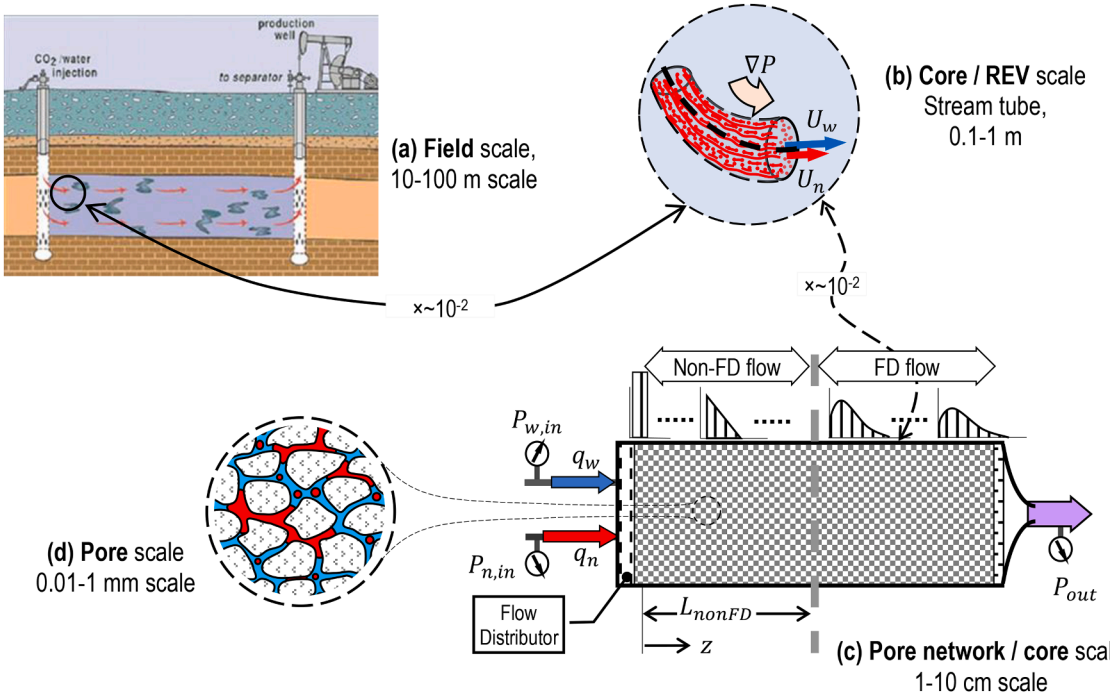


Fig. 1. Typical up-scaling / down-scaling implemented in modeling two-phase flow in porous media. (a) The field scale. (b) The Darcy (or REV stream tube) scale of the fractional flow, constitutive model. (c) The core, or network scale model, and imposed flow conditions; the evolution of the flow structure is exhibited by representative size distributions of the disconnected non wetting phase elements. (d) The pore-scale model whereby the virtual magnification depicts the internal structure of the composite flow within the core of a porous medium at the scale of a few pores; the disconnected non wetting phase (in red) is dispersed within the continuous wetting phase (in light blue).

mechanisms must be described within a hierarchical, multiscale framework. At the pore / microscopic scale, highly nonlinear interactions dominate a variety of intrinsic flow phenomena, whereas at the macroscopic scales flow is typically described within a *representative elementary volume* (REV), where the flow system is treated as an effective mixture of interacting continua. The flow dynamics are primarily controlled by momentum transport associated with two competing mechanisms: capillary forces, arising from interfacial curvature (Young–Laplace / wettability effects), and viscous forces, described by Navier–Stokes flow within the pore network.

The transition from pore-scale to REV-scale relies on spatial averaging (upscaling), whereby the ensemble of interfacial and viscous interactions are integrated into phenomenological constitutive relations. These relations, such as fractional-flow extensions of Darcy's law, link average phase fluxes to pressure gradients and form the basis for continuum-scale modeling and simulation (Dullien, 1992; Bear, 2018). Importantly, the definition of an REV is scale-dependent and problem-specific, particularly in multiscale or multiphysics systems where different flow components may exhibit distinct characteristic sizes and volumetric fractions.

Albeit two-phase flow in porous media is central to a wide spectrum of energy and environmental technologies, its macroscopic description remains fundamentally incomplete. In practice, the phenomenology of steady-state two-phase flow in porous media is recorded in diagrams of relative permeabilities obtained through systematic experimental studies in *Special Core Analysis Laboratory* (SCAL) interventions (Richardson et al., 1952). In these experiments, proxy fluid phases are co-injected through core samples under controlled flow conditions and pressure drops are measured to infer relative permeabilities via generalized (i.e. multiphase) Darcy-type relations, Fig. 1(c). Advanced imaging techniques, including X-ray micro-computed tomography (μXRCT) (Georgiadis et al., 2013; Wildenschild and Sheppard, 2013; Oughanem et al., 2015; Youssef et al., 2017; Andrew et al., 2015; Pak et al., 2015) have further enhanced insight into pore-scale flow structures, enabling direct observation of saturation distributions and dynamic events such as Haines jumps (Berg et al., 2013) or contact angle variations (Singh et al., 2016). Downstream the application pathway, the resulting core-scale REV descriptions are implemented in reservoir simulators for field-scale predictions.

The conventional framework based on fractional extensions of Darcy's law, rooted in saturation-dependent relative permeability functions, is also applied in SCAL measurements that traditionally express relative permeability as a function of phase saturation. However, theoretical inferences (Valavanides and Payatakes, 2001; Valavanides, 2018(b)), supported by numerical (Constantinides and Payatakes, 1989; 2000; Valavanides et al., 1998; Blunt et al., 2002; Nguyen et al., 2006; Sinha et al., 2017; 2021; Valavanides, 2018(a); Yiotis et al., 2019), and experimental evidence (Wyckoff and Botset, 1936; Avraam and Payatakes, 1995; 1999; Wildesrschild et al., 2001; Tallakstad et al., 2009; Datta et al., 2014; Youssef et al., 2014; Rücker et al., 2015; Tsakiroglou et al., 2015; Armstrong et al., 2016; Zou et al., 2018; Gao et al., 2020; Valavanides et al., 2020, Zhang et al., 2021; Karadimitriou et al., 2023), indicate that steady-state flow behavior depends not only on saturation, but also explicitly on flow conditions, particularly in regimes where capillary and viscous forces are comparable, and disconnected non-wetting phase structures (ganglia and droplets) remain mobile through dynamic connectivity in intermittent micro-flows (Reynolds et al., 2017; Spurin *et al.*, 2019; Anastasiou *et al.*, 2024; Wang et al., 2025). The take away message is that widely used relative permeability models based on saturation dependency lack universality and often fail to provide predictive accuracy outside the narrow conditions under which they are calibrated. These findings motivate the development of flow-dependent constitutive models, implementing different upscaling approaches, based on pure mechanistic or hybrid mechanistic-thermodynamic-stochastic analyses (Berg et al., 2026).

SCAL experiments form the cornerstone of industrial practice for characterizing two-phase flow in natural porous media (McPhee, 2015). Yet, a critical challenge in SCAL is the presence of so-called *capillary end effects* (CEE), arising from the abrupt transition from single-phase flow in inlet tubing into two-phase flow within the porous medium. This transition induces a spatial reorganization of the flow structure past the inlet, before a fully developed (FD) state is reached further downstream, Fig. 1(c). Consequently, a non-negligible portion of the core operates under transient or evolving flow conditions (non-fully developed, non-FD), even when macroscopic steady state appears to have been established. Moreover, because capillary pressure must fall to zero where a core meets an open outlet, the wetting phase accumulates (or is depleted) near that face (Leverett, 1941; Osoba et al., 1951; Richardson et al., 1952). The consequence is biased endpoint relative permeabilities, distorted curve shapes near residual saturations, and apparent (but often spurious) rate-dependence of relative permeability (Chen and Wood, 2001). This directly violates the underlying premise of REV-scale modeling and introduces a latent bias in measured pressure gradients and inferred relative permeabilities. Despite the efforts to correctly reproduce the real flow conditions (steady-state or transient, drainage or imbibition, confining / overburden pressure and temperature) as well as system properties (viscosity ratio, wettability and other physicochemical properties of the proxy fluids), CEE pose an inherently critical problem in SCAL. They bias the interpretation of any relation between the measured values of the physical quantities (pressure gradients, saturation and flow-rates), thereby compromising the validity of the inferred REV-scale constitutive relations. End effects may be substantial or not, depending on the extent of the non-FD zone relative to the core length. Their magnitude depends on flow conditions, fluid properties, as well as pore network characteristics and overall length, and they are particularly pronounced in low capillary number regimes.

In this context, end effects can compromise the trueness of REV-scale constitutive relations that are implemented in field-scale simulators. End effects are typically regarded as experimental artefacts to be minimized.

To reduce their impact, longer cores are used or high injections flowrates are imposed, albeit this is not always technically possible. In general SCAL measurements are deployed with the objective to estimate critical parameters of the formation specimen (core), e.g. relative permeability and capillary pressure. Two main methods of SCAL experiments are steady-state and unsteady-state.

In steady-state (SS) the fluids are co-injected at fixed fractional flow until conditions stabilize, then the the Darcy law is applied directly (Richardson et al., 1952; API, American Petroleum Institute 1998). The method is reliable in principle, but vulnerable to end effects unless the core is long or the rate high enough that the affected zone is a small fraction of the core (Rapoport and Leas, 1953). This mitigation-by-design approach has practical limits: long cores are costly, and high rates risk introducing genuine rate-dependent effects that mimic the CEE (Chen and Wood, 2001; Peksa et al., 2015). In steady-state methods correction routes use the independently measured capillary pressure curve directly (Huang and Honarpour, 1998). Virnovsky et al. (1995) developed an early method that explicitly accounts for capillary end effects (CEE) by retaining the capillary-pressure term in steady-state equations. The method requires varying total flow rate and phase-flow-rate ratio to determine saturation and relative permeability at a reference location, rather than assuming uniform core-average saturation. A dominant analytical correction is the intercept method: plotting average saturation and inverse effective relative permeability against inverse total flow rate and extrapolating the high-rate linear trend to infinite rate removes the end-effect bias (Gupta and Maloney, 2015; 2016). Andersen et al. (2017, 2020, 2021) derived this analytically for Corey-type functions (Brooks and Corey, 1964), introducing a capillary number governing how much of the core is end-affected. Goodarzian and Sorbie (2023) refined the underlying pressure-drop relationship. Reed and Maas (2018) validated the method across multiple case studies. Other correction routes use a stability factor

derived from paired flow-rate experiments. A more recent, contrasting view treats the CEE not as noise but as information: because fractional flow is constant along the core at steady state, local pressure gradients within the end-affected zone can, with in-situ saturation imaging, yield relative permeability from a single test (Zou et al., 2020). Bedrikovetsky and coworkers pursue a closely related strategy through the steady-state-transient test (SSTT): rather than discarding the transition data between successive fractional-flow steps, they use the stabilization-time and pressure-drop transients — governed by the saturation-diffusion coefficient in the Rapoport–Leas equation — to back out relative permeability and capillary pressure jointly from a single coreflood; they implement this for water–oil and gas–water systems (Borazjani et al., 2021a, 2021b) and for mixed-wet rocks and CO_2–water systems (Hemmati et al., 2024).

Interpretation of SCAL measurements under unsteady-state (USS) methods is faster, using transient production/pressure data with fractional-flow theory (Buckley and Leverett, 1942; Welge, 1952; Johnson et al., 1959). The JBN method assumes negligible capillary and gravitational forces, valid only at high viscous-to-capillary ratios (Rabinovich et al., 2019). Consequently, its reliability is questioned in tight rocks, at low rates, or near residual saturations, precisely where end effects are strongest. Modifications reintroduce capillary physics, as Chen and Wood's (2001) extended JBN, and Al-Sarihi et al. (2020) incorporates capillary-pressure boundary conditions, while Cao et al. (2014) presented a constant-pressure-boundary analytical alternative. Recently, a capillary end-effect correction method for relative permeability curves was developed, using optimized models and saturation profiles for reservoirs with varying porosity and permeability (Li et al., 2025).

Because analytical corrections rest on simplifying assumptions, the industry standard has switched on numerical inverse modelling: simulating the coreflood with correct geometry and boundary conditions, then tuning relative permeability and capillary pressure functions until simulated and measured pressure, production, and (where available) saturation-profile data match (Sigmund and McCaffery, 1979; Kerig and Watson, 1986; Grattoni and Bidner, 1990; Tsakiroglou et al., 2004; Masalmeh et al. 2014). Maas and coworkers developed widely used commercial SCAL interpretation software built on this inverse-modelling philosophy (Maas and Schulte, 1997; Lenormand et al., 2016; Maas et al., 2019; Nono et al., 2019). A persistent limitation is non-uniqueness — multiple parameter sets can fit the same data equally well — motivating Bayesian and ensemble-based uncertainty--quantification frameworks (Subbey et al., 2003; Zhang et al., 2012; Berg et al., 2021; Almutairi et al. 2022, Ge et al., 2022;Dell'Oca et al., 2023; An et al., 2023). Yet the practicality of simultaneously determining both relative permeability and capillary pressure from one experiment is questionable, since instrument resolution near the inlet/outlet faces is weakest exactly where CEE information is concentrated; independently measuring capillary pressure (e.g., by centrifuge) remains the recommended practice. To address this problem Bedrikovetsky and coworkers developed an inverse-solver framework for steady-state-transient test (SSTT) and regularize the inverse problem using the shape (U- or S-shaped) of the stabilization transients rather than an independently measured capillary pressure curve (Borazjani et al., 2021a, 2021b; Hemmati et al., 2024).

Machine learning and digital rock physics are a growing frontier: physics-informed ML and reinforcement-learning frameworks now estimate relative permeability and capillary pressure parameters from coreflood time series (Kalule et al., 2026).

Bottom line - The principal distinction is between methods that neglect CEE, methods that correct for it analytically, and methods that represent it explicitly in an inverse numerical model: For high-quality SCAL data, the strongest practice is generally not to discard JBN or conventional steady-state interpretation, but to use them as initial/reference solutions and then quantify the CEE through a multi-rate analytical correction or a numerical model incorporating the measured or independently determined capillary pressure vs saturation curve. This is especially important when the capillary number is low, the core is tight, or accurate endpoint relative permeabilities are required.

The present study addresses the problem of capillary end effects by pursuing two objectives: (i) to examine if end effects contribute systematically –and predictably– to the observed flow structure, particularly in low capillary number and low flow rate ratio regimes, and (ii) to investigate whether their signature can be extracted from simple, ex-core measurements alone, bypassing any direct access to interstitial, pore-scale information. In our study we have included explicitly the rate effects, by considering the superficial velocities of the co-injected fluids, in properly dimensionless independent variables, namely the capillary number and the fractional flowrate, based on the hybrid mechanistic-stochastic theoretical framework of *Decomposition in Prototype Flows* (*DeProF*) (Valavanides, 2018(b)).

To achieve this, we extended a precursor study in microfluidic network (Karadimitriou et al., 2023) by decoupling the roles of pore geometry and wettability. To this end we deploy systematic experiments in both periodic and non-periodic microfluidic, planar model pore networks fabricated from different materials. In parallel, we take advantage of the transparency of the matrix material and introduce an imaging-based methodology to resolve the spatiotemporal evolution of flow structures, enabling direct correlation between interstitial flow structure and external measurements. This approach allows us to identify characteristic invariants of the flow and to reinterpret SCAL data within a flow-structure-informed framework consistent with the *DeProF* paradigm (Valavanides, 2023).

When significant end effects and non-fully developed two-phase flow are present, the measured inlet–outlet pressure drop cannot, in general, be attributed solely to a representative elementary volume (REV) under fully developed flow conditions, as it may also include contributions from inlet / outlet channels, fluid redistribution, and developing-flow regions. This limitation is central to the present study. Rather than interpreting the experimentally derived quantities as rigorous REV-scale relative permeabilities, we examine whether ex-core measurements from co-injection experiments can indicate the magnitude and evolution of end effects, particularly near critical flow conditions. Unlike conventional steady-state SCAL experiments, typically performed at sufficiently high capillary numbers to minimize end effects, our experiments span capillary-dominated to viscosity-dominated regimes, with particular emphasis on the critical conditions identified by the DeProF framework. Accordingly, the pressure-derived quantities reported here should be regarded as effective or apparent flow parameters characterizing the experimental domain, rather than as intrinsic REV-scale relative permeabilities when significant end effects are present.

Our study provides evidence that end effects are integral components of the observed flow response, with measurable impact on REV-scale constitutive relations. This challenges the conventional interpretation of SCAL measurements in terms of saturation dependency and calls for a revision of standard protocols, accounting for flow rate dependency of relative permeabilities. In parallel, it establishes a pathway to infer flow-structure information from macroscopic observables, and contributes toward the development of flow-dependent, true-to-mechanism relative permeability models with improved specificity.

The paper is organized in 4 sections, including this introductory section. Section 2 provides the theoretical framework, i.e. a basic analysis of steady-state, two-phase flow in porous media, and a discussion on the concept of fully-developed flow conditions and end effects when porous media specimens of finite length are examined. Section 3 describes the materials and laboratory workflow of the experiments. Section 4 presents the results of study and discusses the potential for improving SCAL protocols.

2. Basic theoretical framework

For the self-sufficiency of the current work, we present here the basic

theoretical framework, developed by Valavanides (2018b, 2023) for the energy and flowrate-dependency analysis of steady-state two-phase flow in pore networks.

2.1. Basic considerations

Consider the simultaneous, one-dimensional concurrent flow of a non-wetting phase (NWP), and a wetting phase (WP), both incompressible through a porous medium (PM). The variables pertaining to the NWP are indexed with *n*, whereas those pertaining to the WP are indexed with *w*. Note, a tilde (~) embellishment indicates a dimensional variable, otherwise the variable is dimensionless.

The two phases flow across a porous medium control surface with cross-sectional area, $\widetilde{A}$, with flow rates $\widetilde{q}_n$ and $\widetilde{q}_w$, respectively. Average corresponding pressure gradients, $(\Delta\widetilde{p}/\Delta\widetilde{z})_w$ and $(\Delta\widetilde{p}/\Delta\widetilde{z})_n$ are induced upon the two phases. The term "average" refers to the representative elementary volume (REV) average. This type of two-phase flow is described by the set of phenomenological, fractional flow, Darcy-type relations,

$$\frac{\widetilde{q}_n}{\widetilde{A}} \equiv \widetilde{U}_n = \frac{\widetilde{k}}{\widetilde{\mu}_n} k_{rn} \left(\frac{\Delta\widetilde{p}}{\Delta\widetilde{z}}\right)_n \text{ and } \frac{\widetilde{q}_w}{\widetilde{A}} \equiv \widetilde{U}_w = \frac{\widetilde{k}}{\widetilde{\mu}_w} k_{rw} \left(\frac{\Delta\widetilde{p}}{\Delta\widetilde{z}}\right)_w \tag{1}$$

where,

$\widetilde{U}_w, \widetilde{U}_n$ are the superficial velocities, $\widetilde{\mu}_w$, $\widetilde{\mu}_n$ are the dynamic phase viscosities, and $\widetilde{k}$ is the absolute (intrinsic) permeability of the pore network.

The flow rate ratio of the two phases, *r*, is defined as,

$$r = \widetilde{q}_n/\widetilde{q}_w = \widetilde{U}_n/\widetilde{U}_w \tag{2}$$

and is essentially a *kinematic* property of the flow.

The mobility ratio, λ, is defined as the ratio of the mobilities,

$$\lambda = \frac{\widetilde{\lambda}_n}{\widetilde{\lambda}_w} = \frac{(k_{rn}/\widetilde{\mu}_n)(\Delta\widetilde{p}/\Delta\widetilde{z})_n}{(k_{rw}/\widetilde{\mu}_w)(\Delta\widetilde{p}/\Delta\widetilde{z})_w} = \frac{1}{\kappa}\frac{k_{rn}}{k_{rw}}\frac{(\Delta\widetilde{p}/\Delta\widetilde{z})_n}{(\Delta\widetilde{p}/\Delta\widetilde{z})_w} \tag{3}$$

and is essentially a *kinetic* property of the flow as it relays to the pressure gradients, $(\Delta\widetilde{p}/\Delta\widetilde{z})_i$, $i = n,w$. where the NWP/WP bulk viscosity ratio, κ, is defined as

$$\kappa = \widetilde{\mu}_n/\widetilde{\mu}_w \tag{4}$$

The average intrinsic capillary pressure is

$$\widetilde{p}_c(\widetilde{z}) \equiv \widetilde{p}_n(\widetilde{z}) - \widetilde{p}_w(\widetilde{z}) \tag{5}$$

where $\widetilde{p}_n(\widetilde{z})$, $\widetilde{p}_w(\widetilde{z})$, are the average bulk pressures in the NWP and WP respectively (see also (Valavanides, 2023, Appendix I). This definition is in line with the definition provided by Bear (2018, Eq. 6.1.1). Note that Eq. (5) provides a measure of the capillary pressure jump across the two bulk phase pressures due to the combined effect of Young-Laplace capillary forces acting across all NWP/WP menisci. So long as the NWP is disconnected, to a larger or smaller extent, $\widetilde{p}_c(\widetilde{z}) > 0$.

2.2. Non-fully and fully developed flow

When the fluids are co-injected at constant (but generally different) flow-rates, they gradually evolve from uncoupled, single phase Poisseuille-type flow within the injecting tubes, to a complex two-phase network-flow system. Downstream the inlet ports, the NWP disconnects into fluidic elements, i.e. ganglia of relatively large or small size and/or droplets (see e.g. Anastasiou et al., 2024), that interact with each other and the WP by exchanging momentum across their interfaces. The interstitial structure of this flow system can be described by an evolving size distribution of disconnected NWP fluidic elements (ganglia, droplets), Fig. 1(c) (Valavanides et al., 1998). The interstitial flow structure at any position downstream the entry ports can be described – at increasing levels of resolution – by saturation, fractional flows of droplets, ganglia and connected pathways (i.e. super-long or percolating ganglia) and ganglion size distributions (Valavanides, 2018(a)). The local flow at any cross-section takes a steady-state, time-average configuration, described by an ensemble of incessant, instantaneous *physically admissible flow configurations* or *flow microstates*(Valavanides and Daras, 2016, Valavanides, 2018(a)). As it evolves downstream the inlet ports, it is *non-fully developed*. If the network, or the core, is adequately long and relatively homogeneous, then, far downstream the inlet ports, the flow system will eventually reach a *fully developed* state, where the partitioning of NWP among the above-mentioned configurations remains practically constant with both time and along the main flow direction. Attaining a fully developed state is not always possible. That depends on the combination of the flow conditions, the physico-chemical properties of the fluids and the structure of the pore network. Most critical is the role of the relative magnitude of the viscous forces over capillary forces, and the heterogeneity properties of the network. Exhibits of transitions of interstitial flow from non-fully developed to fully-developed structures can be found in Aursjo et al. (2014).

When the flow system has reached a fully developed (FD) state, the local capillary pressure remains constant and the two local pressure gradients pertaining to the NWP and the WP, become equal,

$$\textit{fully developed flow}: \left(\frac{\Delta\widetilde{p}}{\Delta\widetilde{z}}\right) \approx \left(\frac{\Delta\widetilde{p}}{\Delta\widetilde{z}}\right)_w \approx \left(\frac{\Delta\widetilde{p}}{\Delta\widetilde{z}}\right)_n \tag{6}$$

Therefore, the phenomenological, Darcy type, fractional flow relations that describe the steady-state fully developed flow become,

$$\frac{\widetilde{q}_n}{\widetilde{A}} \equiv \widetilde{U}_n = \frac{\widetilde{k}}{\widetilde{\mu}_n} k_{rn} \left(\frac{\Delta\widetilde{p}}{\Delta\widetilde{z}}\right) \text{ and } \frac{\widetilde{q}_w}{\widetilde{A}} \equiv \widetilde{U}_w = \frac{\widetilde{k}}{\widetilde{\mu}_w} k_{rw} \left(\frac{\Delta\widetilde{p}}{\Delta\widetilde{z}}\right) \tag{7}$$

and, under such conditions, the common pressure gradient in both phases can be expressed in reduced form,

$$x = \frac{\Delta\widetilde{p}/\Delta\widetilde{z}}{(\Delta\widetilde{p}/\Delta\widetilde{z})^{1\Phi}} = \frac{\Delta\widetilde{p}}{\Delta\widetilde{z}}\frac{\widetilde{k}}{\widetilde{\mu}_w\widetilde{U}_w} = \frac{\Delta\widetilde{p}/\Delta\widetilde{z}}{\widetilde{\gamma}_{nw}Ca/k} = \frac{\Delta\widetilde{p}}{\Delta\widetilde{z}}\frac{\widetilde{k}}{\widetilde{\mu}_w\widetilde{U}_w} = \frac{1}{k_{rw}} \tag{8}$$

where

$(\Delta\widetilde{p}/\Delta\widetilde{z})^{1\Phi}$ is the pressure gradient corresponding to an equivalent saturated single-phase flow (1Φ) of the WP at the same superficial velocity $\widetilde{U}_w$

Ca is the capillary number, conventionally expressed as

$$Ca = \frac{\widetilde{\mu}_w\widetilde{U}_w}{\widetilde{\gamma}_{nw}} \tag{9}$$

where $\widetilde{\gamma}_{nw}$ is the interfacial tension between the two phases. This particular expression is only nominal; it fails to capture the true physics behind the definition of the capillary number, as the ratio of the viscous to the capillary forces, especially when both phases are mobile. Please note that this expression is strict /correct only when the saturation of the NWP is approaching zero and the sparse disconnected NWP elements are immobile. In case of two-phase flow, the expression in Eq. (9) fails to account for the viscous forces, from the bulk flow of both phases, as well as the effective capillary forces due to the motion of the n/w menisci through the tortuous network. The issue has been discussed in Valavanides (2018b) where he introduced the concept of an effective capillary number, and recently by Yang et al. (2026).

Note that, by definition, the reduced pressure gradient is essentially the inverse of the relative permeability of the WP [see far right side of Eq. (8))]. Moreover, the set of superficial velocities in Eq. (7) may be appropriately reduced and replaced by a set of dimensionless variables, namely, the capillary number, *Ca*, Eq. (9), and the NWP/WP flow-rate ratio, *r*, Eq. (2).

At steady-state conditions, if and only if the flow is fully developed (FD), i.e. there are either no capillary end effects or these can be

considered to be negligible, the flow-rate ratio, r, becomes equal to the mobility ratio, λ.

$$FD\ flow:\ r = \frac{U_n}{U_w} \equiv \frac{1}{\kappa}\frac{k_{rn}}{k_{rw}} = \lambda \ \Leftrightarrow\ k_{rn} = \kappa r k_{rw} \tag{10}$$

In fully developed flows, because of the common pressure gradient, Eq. (7) or (8) and the equivalence between flow-rate ratio and mobility ratio, Eq. (10)), relative permeability curves intersect at a fixed value of the flow-rate ratio, the so-called relative permeability cross-over value, r_x. The latter is equal to the inverse of the viscosity ratio (Valavanides, 2023],

$$r_x = 1/\kappa \tag{11}$$

This inherent characteristic of steady-state, fully developed flows, Eqs. (10) and (11), may be used in assessing the presence of capillary end effects when reviewing relative permeability data collected during SCAL. If the imposed flow-rate ratio values, r_i, and the corresponding measured mobility ratio values, λ_i, are equal, then fully developed flow conditions have settled-in and end effects are considered to be negligible. Ideally, in absence of end effects, then, all pairs of $\{r_i, \lambda_i\}$ align on a straight line with inclination 1:1. In practice, when SCAL measurements are examined, the equality expressed by Eq. (10), could be used as a soft criterion in verifying the absence or negligibility of end effects. We have applied this criterion in the current study.

2.3. Energy efficiency & independent variables

The energy efficiency of the process is defined (Valavanides, 2018b) as the flow-rate of the NWP per unit of total hydraulic power spent, or equivalently, provided externally to the NWP/WP/PM system by the injection pumps, to maintain two-phase flow at any set of externally imposed flow conditions, i.e., Ca and r. The associated *energy efficiency index,* f_{EU}, can be readily calculated in terms of macroscopic measurements, as

$$f_{EU} = \frac{k_{rn}}{\kappa(r+1)} = \frac{rk_{rw}}{r+1} = \frac{r}{x(r+1)} \tag{12}$$

An important characteristic of two-phase flow in porous media is that for every fixed value of the capillary number, Ca, there exists a single value of the flow-rate ratio, r^*, for which the energy efficiency index, $f_{EU}{}^*$, attains a maximum value (Valavanides et al., 2016). Moreover, for every two-fluid / pore network system, a unique locus of energy efficiency maxima is formed, $r^*(Ca)$. The flow conditions that correspond to the $r^*(Ca)$ locus and minimize the total energy dissipation per unit of NWP flow-rate, are called *critical flow conditions* (CFCs). The critical energy efficiency index, $f_{EU}{}^*(Ca)$, and the associated locus of CFCs, $r^*(Ca)$, provide a strong tool for flow analysis and characterization (Valavanides, 2018b).

2.4. Universal relative permeability scaling form, incorporating flow-rate dependency

The *DeProF* (Decomposition in Prototype Flows) model is a hybrid mechanistic-stochastic model for predicting the dimensionless macroscopic pressure gradient, x, in immiscible, steady-state two-phase flows through pore networks. It integrates pore-scale interfacial dynamics and network-scale cooperative phenomena to estimate the effective conductivity of different pore unit cell classes in a stochastic approach. Utilizing effective medium theory and ensuring pore-to-macro-scale consistency for non-wetting and wetting phase mass transport, *DeProF* formulates an implicit algebraic expression linking x to key system and flow parameters: capillary number, Ca, flow-rate ratio, r, viscosity ratio, κ, dynamic advancing and receding contact angles (θ_A, θ_R), and a set of parameters describing pore network geometrical and topological characteristics. Extensive simulations with the *DeProF* model algorithm have mapped the flow regime dependencies across five orders of magnitude in Ca and r, for nine different viscosity ratios (Valavanides, 2018a).

Based on the *DeProF* simulations it was possible to infer a universal description of the dependence of the reduced pressure gradient, $x(Ca,\ r)$, on the capillary number, Ca, and the flow-rate ratio, r, expressed by the universal scaling form (Valavanides, 2023),

$$x(\log Ca, \log r) = A(\log Ca) + \kappa r \tag{13}$$

whereby the effects of capillarity and viscosity are partitioned in two decoupled terms. The linear term describes the fractional contribution of the bulk viscosities through the viscosity ratio, κ. The non-linear term, $A(\log Ca)$, is the *Intrinsic Dynamic Capillary Pressure (IDCP)* function; it accounts the capillarity effects associated to the physicochemical properties of the two-fluid system and the pore network, i.e. wettability (dynamic receding and advancing contact angles) and pore network geometry, at different flow conditions. In particular, the *IDCP* function, $A(\log Ca)$, is a *characteristic property* of the NWP/WP/PM flow system. The term *dynamic* in IDCP is used to indicate that capillary pressure is evaluated at different flow conditions – not in static equilibrium (Valavanides, 2023).

In the present work, we perform a SCAL study and recover the IDCP function, $A(\log Ca)$, specific to the two-fluids/pore network systems under consideration.

3. Materials and methods

3.1. Microfluidic model networks and fluids

Three model pore networks were used in the study. All micromodels are 2,5D planar with a three-dimensional pore structure. The pore structure of the median plane section of the micromodels is exhibited in Fig. 2. Two of the network models have a periodic structure (see following paragraphs), one is non-periodic. For quick reference, the codification of the network geometry is “P” for periodic and “NP” for non-periodic.

Two of the model pore networks (denoted as PDMS-P and PDMS-NP) were produced using Poly-Di-Methyl-Siloxane (PDMS) implementing optical and soft lithography techniques (Xia and Whitesides, 1998; Karadimitriou et al., 2013). The third model pore network (denoted as Glass-P) was produced using glass by chemical etching techniques (Wegner and Christie, 1983; Avraam, et al., 1994).

The three model networks are referenced by combining the attributes to the matrix material and the periodicity characteristics, i.e. PDMS-P, Glass-P and PDMS-NP (Fig. 2).

The pore network in the PDMS-P and Glass-P models is periodic in both principal orthogonal directions; it is made by tiling-up a basic network element in both directions; 3 periods along the longitudinal axis which is also the superficial flow direction, and 2 periods across the transverse axis. The pore size range is [75–250] μm, with a mean size equal to 180 μm. That range pertains to the diameters of circles inscribed in the various pores; the latter comprise the void space between the aforementioned cylindrical pillars (“grains”). Because of the particular geometric configuration there is no clear /nominal characterization of pore bodies as “chambers” or “throats”. A conventional dimensional delimiter could be the average diameter of inscribed circles; any pore with larger nominal diameter could be considered as chamber, whereas a pore with smaller nominal diameter as throat. As per connectivity, there are no dead-end pores, apart those residing at the sides of the network –parallel to the longitudinal flow direction.

The PDMS-NP geometry is designed following a standard spectral method, where a matrix of independently distributed Gaussian random numbers is generated in a 2D regular grid and transformed into the (spatial) frequency domain using a 2D Fast Fourier Transform (FFT) (see e.g. Yiotis et al., 2019). A spectral filter, derived from the Fourier transform of the selected covariance model, is then applied to impose

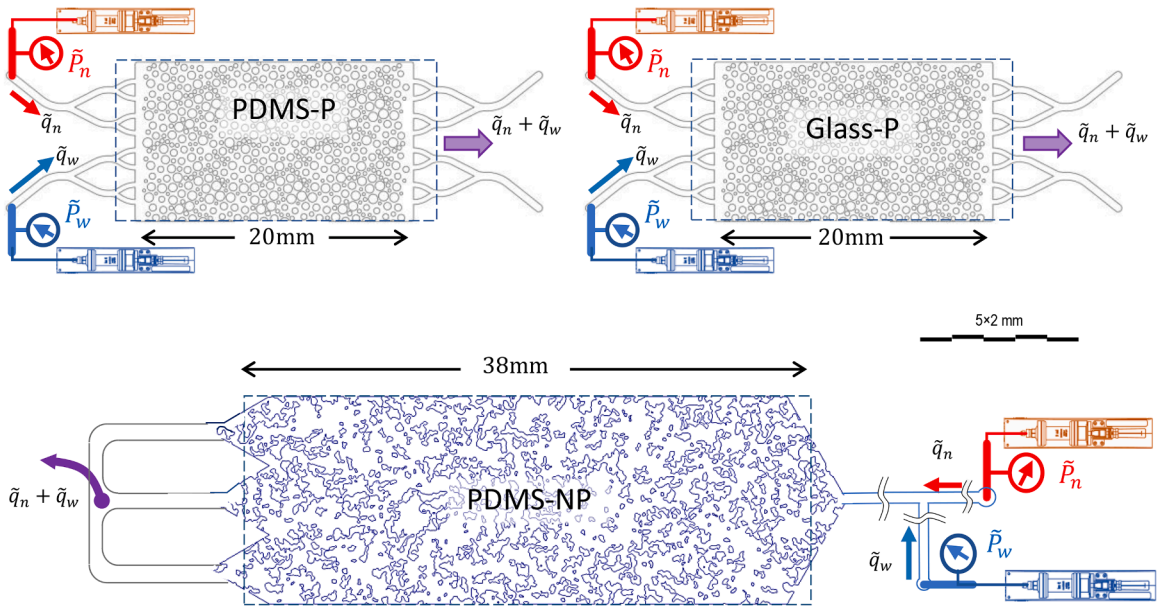


Fig. 2. Mid-plane section of the microfluidic networks (in-scale) used in the co-injection experiments and schematics of the syringe pumps. The fluids are co-injected through the inlet micro-channeling and the immiscible flow is collected at the exit. Top: the periodic (P) networks made of PDMS and glass; bottom: the non-periodic (NP) network made of PDMS.

the target spatial correlation. Depending on the selected model, the resulting structure is controlled by a characteristic correlation length(s), λ_S, and, where applicable, additional shape or smoothness parameters, which govern the continuity, roughness, and multi-scale character of the solid phase. The filtered field is inverse FFT-transformed to real space to obtain spatially correlated values (i.e., a latent continuous random field). A threshold based on the target porosity, φ, is then applied to classify voxels as solid (1) or void (0) and to thus generate binary pore structure (simulated porous medium). For this contribution, we employ an exponential spatial correlation kernel with a correlation length equal to 350μm. The top-view porosity of the domain is set equal to $\varphi = 0.7$, while the average obstacle size is 0.14mm^2 and the media is 0.027mm^2.

Due to the different manufacturing processes between the PDMS and Glass networks, there are differences in the out-of-plane layout of the pore (void) network. Both the PDMS networks (PDMS-P and PDMS-NP) have an orthogonal geometry. In the PDMS-P network circles correspond to the planar cross-sections of the PDMS cylinders (solid pillars of circular cross-sections) connecting the two parallel plates confining the flow. In the PDMS-NP network, the vertical pillars connecting the two horizontal plates (bottom and top) have a prismatic geometry of irregular cross-section. In that context, any cross-section perpendicular to the horizontal (mid-) plane in any the two PDMS networks comprises orthogonal sections of void and solid spaces. The effective, overall dimensions of the PDMS-P network are 10 mm × 20 mm. The depth of the porous structure, in the PDMS-P and PDMS-NP networks is constant throughout the entire pore space and the surface is smooth. The depth in the Glass-P network has some degree of irregularity with surface micro-roughness due to the implemented chemical etching technique. The basic geometric configuration of the three models is given in Table 1.

The absolute permeabilities of the three networks, taking into account the inlet/outlet micro-channel network, were measured by injecting a single phase and implementing the saturated flow Darcy expression. Measured values of absolute permeabilities are given in Table 1. Together with the average void surface of the cross section (perpendicular to flow).

The two immiscible fluids are injected through the inlet micro-channeling with predetermined fluxes, $\tilde{q}_n$, $\tilde{q}_w$. The immiscible flow exits the network through the outlet micro-channeling at atmospheric pressure.

Table 1
Basic geometric configuration of the three model networks used in the study.

Network geometric properties	PDMS-P	Glass-P	PDMS-NP
Length, $\tilde{L}$ [mm]	20	20	38
Width [mm]	10	10	13
Depth [μm]	43	~36	56
Nominal height of chip plate [μm]	54	45	70
Average surface cross-section (void), $\tilde{A}$ [m^2]	4.3×10^{-7}	$\sim 3.5 \times 10^{-7}$	1.4×10^{-7}
Median plane area porosity	0.45	0.45	0.7
Abs. Permeability, $\tilde{k}$ [m^2]	1.18×10^{-11}	0.68×10^{-11}	1.04×10^{-11}

The fluids used in the experiments were deionized water dyed with ink, and Fluorinert^{TM} FC-770. The basic physicochemical and wettability properties of the fluids are presented in Table 2. The addition of the dye in water has practically no effect on its viscosity and density, as confirmed by relevant measurements. Note that the wettability of the two fluids changes with the material of the network matrix (solid phase), i.e. PDMS is hydrophobic and wetted by the Fluorinert^{TM} FC-770, whereas Glass is hydrophilic and wetted by the dyed water. Wettability of the two-fluid and pore network system is described by the dynamic advancing, θ_A, and receding, θ_R, contact angles. Nominal values have been roughly estimated from visual observations of the recorded snapshots. Contact angles measured in two-dimensions are approximate

Table 2
Basic physicochemical properties of the proxy fluids used in the study.

Fluids & physicochemical properties	Density $\tilde{\rho}$ [kg/m^3]	Dynamic viscosity $\tilde{\mu}$ [mPas]	Interfacial tension $\tilde{\gamma}_{nw}$ [N/m]	Solid	
				PDMS	Glass
Fluorinert^{TM} FC-770	1793	1.359	55×10^{-3}	WP	NWP
Deionized Water + Dye	1000	1.00		NWP	WP
Advancing cont. angle, θ_A [deg]				54 ± 5	41 ± 3
Receding cont. angle, θ_R [deg]				45 ± 5	35 ± 4

and are used as qualitative indicators of the wettability conditions of the system (Ruth, 2020).

The present study is designed as an initial systematic investigation using categorical comparisons of network type, wettability, inlet distributor configuration, and flow conditions, rather than an exhaustive parametric study. Such a study would require an impractically large experimental matrix. The objective is to identify qualitative trends and potentially generic relationships while establishing which variables and interactions are most influential. A more extensive study using systematically matched geometries and materials will be required to quantitatively isolate the effects of network periodicity, geometry, and wettability.

3.2. Experimental set-up and procedure

The experimental set-up is identical to that already used in the precursor study using the PDMS-P network (Karadimitriou et al., 2023). The two fluids were co-injected independently at predetermined volumetric fluxes, using two CETONI^{TM}, neMESYS 1000 N, DC-motor driven syringe pumps, combined with a BASE120 module. Inlet pressures per phase were measured with a set of Elveflow^{TM} MPS sensors, depending on the values of the expected pressure build-up during the injection and the desirable /acceptable measurement accuracy. Both syringe pumps, and logging of the pressure readout values were controlled with QMix-Elements^{TM}. Sampling and recording of the pressure values at the inlet port for each phase was set at rates of 10 Hz. The entire flow system was visualized using an open-air microscope, with a monochromatic camera, Basler^{TM} 5 Mpx, 23 fps, acA2440-20 gm. The purpose of visualizing the interstitial flow was for cross-checking between the structure of the flow, the read-outs from the pressure transducers, and the injected fluxes, in order to trace when the interstitial flow has reached steady-state (see procedure cycle steps in the following paragraph). Snapshots of the interstitial flow structure were captured at frame rates between 15 and 1 Hz, depending on flow conditions. The resolution was set at 8μm/pixel, adequate to observe pore-scale events.

The procedure followed for each *experiment* included a complete cycle of co-injecting the two phases at constant WP volumetric flow-rate, but with successive increases of the NWP flow-rate. The protocol followed was identical for all experiments in the three model networks as in the precursor study (Karadimitriou et al., 2023). For every *i*-experiment a fixed capillary number value, Ca_i, is maintained, whereas the flow-rate ratio takes successive *j*-step-up values, r_j. The domain of flow conditions covered in the experiments is depicted in Fig. 3. A total of 44 constant-*Ca* experiments were performed; 13 in the PDMS-P ($i = \{1,\ldots,13\}$), 19 in the Glass-P ($i = \{1,\ldots,19\}$), and 13 in the PDMS-NP ($i = \{1,\ldots,13\}$), model networks, covering a range of 3×3 orders of magnitude on *Ca* and *r* values. In that context our experimental investigation is similar to the Virnovsky–Skjæveland method (Virnovsky et al., 1995).

The typical cycle in every i-experiment comprises the following steps:

1. The micromodel is initially fully saturated with the WP.
2. The WP is injected at a fixed volumetric flow-rate in order to maintain a constant value of the capillary number, Ca_i, during the entire cycle of the experiment.
3. The volumetric flow rate of the non-wetting phase (NWP) is initially set to approximately one-tenth of that of the wetting phase (WP). It is then increased in successive steps (approximately 9–12 increments). After each incremental increase in the NWP flow rate, sufficient time is allowed for the interstitial flow to attain steady-state conditions. Steady state is identified when the time-averaged pressures of both phases exhibit kinetic stabilization, characterized by small oscillations around constant mean values (Fig. 4). Subsequently, the interstitial flow is visually evaluated in terms of saturation and pore-scale dynamics to confirm stabilization or to verify that any remaining fluctuations follow a consistent, short-period cycle. Following this assessment, the volumetric flow rate of the NWP is further increased in a stepwise manner.
4. After successive repeats with progressive stepwise increments of the flow-rate of the NWP, until a flow-rate ratio value $r \geq 10$ is reached, the experiment for that constant-*Ca* value stops.
5. The system is then reconfigured and a new cycle is deployed pertaining to a new *Ca* value.

Please note that in step 3, the identification of the stabilized flow state was based on the simultaneous assessment of the temporal evolution of the inlet pressures and the video sequence of microscopic images. Because the experiments were conducted under a wide range of flow conditions, the magnitude and character of the fluctuations varied substantially between regimes, see Fig. 5 through Fig. 7. The stabilization criterion therefore involved both pressure behavior and the visual persistence of a statistically similar flow pattern, rather than a single universal numerical threshold. The onset of stabilization following each flowrate ratio step-up is clearly visible in afore mentioned pressure diagrams, especially so for the co-injections at higher capillary numbers. We acknowledge that this procedure contains an element of experimental judgment. Yet, since the experiments were performed by the same operator, using the same procedure, and following the same protocol, the resulting assessment is internally consistent across the experimental campaign.

3.3. Data logging and management

For each run at constant $\tilde{q}_n$ and $\tilde{q}_w$ the values of flow-rates and gauge pressures at the inlet ports for each phase, were sampled and recorded (as described in 3.2). A typical evolution of the two flow-rates and pressures at the inlet ports is depicted in the diagram in Fig. 4. Please note that, the time axis (horizontal) and the flux axis (vertical, right) are

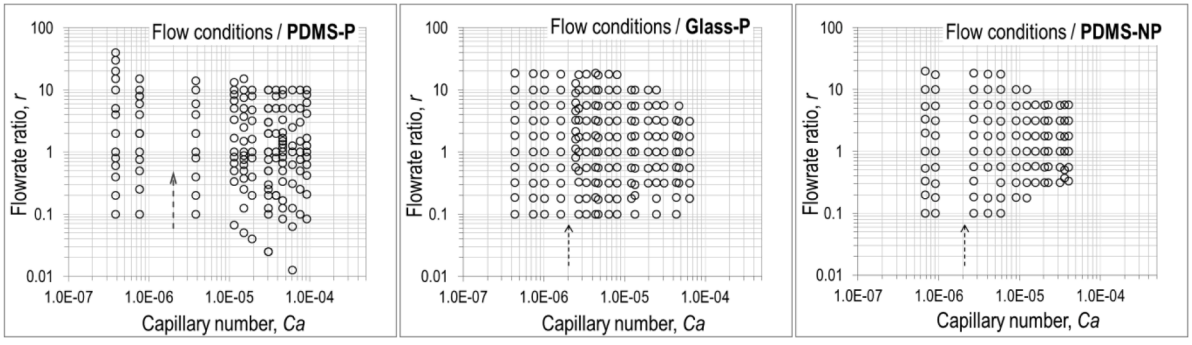


Fig. 3. The domains of steady-state flow cond alitions examined in the study. Markers indicate values of the capillary number, $\boldsymbol{Ca_i}$, and flow-rate ratio, $\boldsymbol{r_j}$. The dashed arrow indicates the direction of increase of the flow-rate of the NWP (at fixed $\boldsymbol{Ca_i}$) for all experiments.

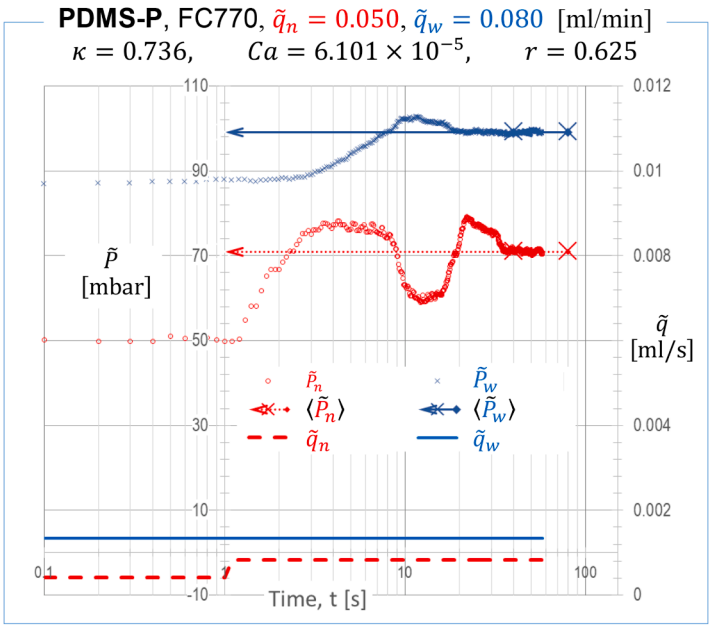


Fig. 4. Typical, time evolution of the inlet pressures (circle and cross markers, left axis) for a typical co-injection of the two phases at predetermined volumetric flow-rates (dashed lines, right axis). The two arrows indicate the time averaged pressures when the flow has reached steady-state. Please refer to the main text for details.

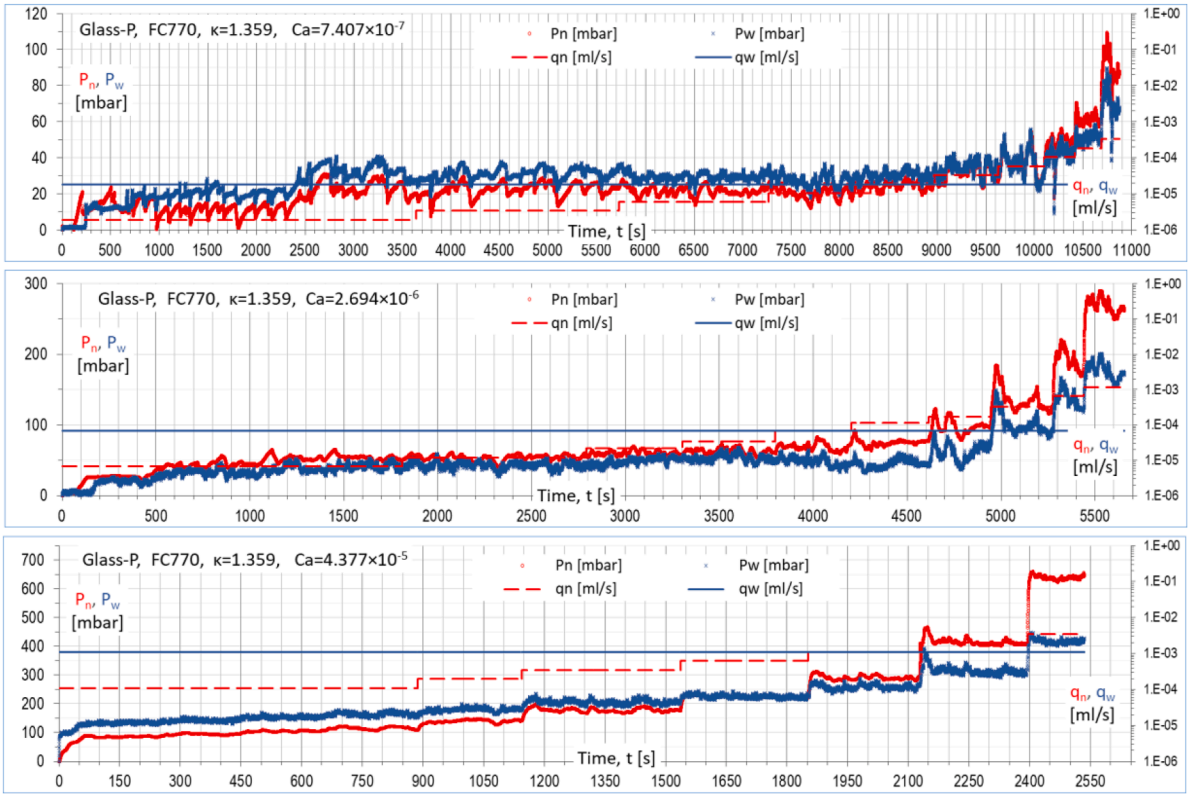


Fig. 5. Typical, time evolution diagrams of pressures ($\tilde{p}$) and flowrates ($\tilde{q}$), pertaining to experiments of steady-state co-injection at 3 different ***Ca*** in the Glass-P network. The measured pressures at the inlet ports are indicated by the small circle markers (red, ◯) for the NWP, $\tilde{p}_n$, and by the small cross markers (blue, ×) for the WP, $\tilde{p}_w$. The compact line (blue, ⟝⟞) indicates the WP volumetric flow rate, $\tilde{q}_w$ dashed line (red, ⟝ ⟞) for the NWP, $\tilde{q}_n$.

logarithmic whereas the pressure axis (vertical, left) is linear.

Pressure values are indicated by markers; flow-rates are indicated by lines. In particular, pressure values measured at the inlet port are indicated by the small circle markers (red, ◯) for the NWP and by the small cross markers (blue, ×) for the WP. The compact line (blue, ——) indicates the volumetric flow-rate for the WP, $\tilde{q}_w$, and the dashed line (red, - -) for the NWP, $\tilde{q}_n$. The step in the NWP line indicates the imposed increase in volumetric flow-rate succeeding the previous co-injection set-up. The long horizontal arrows, pointing to the pressure axis on the left, indicate the average pressure values, or "endpoint

pressure values", calculated when interstitial steady-state conditions settle-in. Time-averaging is taken over the time interval delimited by the two pairs of large crosses over a selected interval, delimited by the two cross markers (×), red for the NWP and blue for the WP pressures. Delimiting this time interval for every examined flow set-up, $(Ca,\ r)$, follows after identifying some form of stabilization in the corresponding pressure log diagram. Then, the average (endpoint) pressures, $\langle \widetilde{P}_n \rangle$, $\langle \widetilde{P}_w \rangle$, are automatically calculated. Finally, the pressure gradients for the WP and the NWP are then readily calculated as

$$(\Delta\widetilde{p}/\Delta\widetilde{z})_i = \langle \widetilde{P}_i \rangle / L,\ i = n, w \tag{14}$$

Typical, time evolution diagrams, pertaining to entire cycles of constant-Ca experiments in the Glass-P network, are also presented in Fig. 5. Again, the measured pressures at the inlet ports are indicated by the small circle markers (red, ◯) for the NWP, and by the small cross markers (blue, ×) for the WP. The compact line (blue, ⊢⊣) indicates the WP volumetric flow rate, $\widetilde{q}_w$, dashed line (red, ⊢ ⊢) for the NWP, $\widetilde{q}_n$. Please note, the time scale is now linear. As in the diagram in Fig. 4, we may observe a time delay until quasi steady-state conditions settle in after each flow rate step-up.

We may also observe that the magnitude of the pressure fluctuations, as well as the time delay and the minimization of the associated fluctuations, depend on the imposed co-injection flow rates, i.e. the (Ca, r) values. In the three diagrams in Fig. 5, starting from a low capillary flow at $Ca = 7.407 \times 10^{-7}$ (top diagram) and moving to intermediate, capillary/viscous, at $Ca = 2.694 \times 10^{-6}$ (middle), and then to viscous flow, at $Ca = 4.377 \times 10^{-5}$ (bottom), we may observe an (expected) systematic progressive decrease of the aforementioned time delay accompanied by a similar decrease in the magnitude of pressure fluctuations around the endpoint pressure average.

The characterizations "capillary", "capillary/viscous" and "viscous" are not arbitrary; they can be confirmed by referring to the compound diagrams in Fig. 13 whereby the afore referenced Ca values are traced in the initial phase, the growth phase (sharp upward slope in the middle)

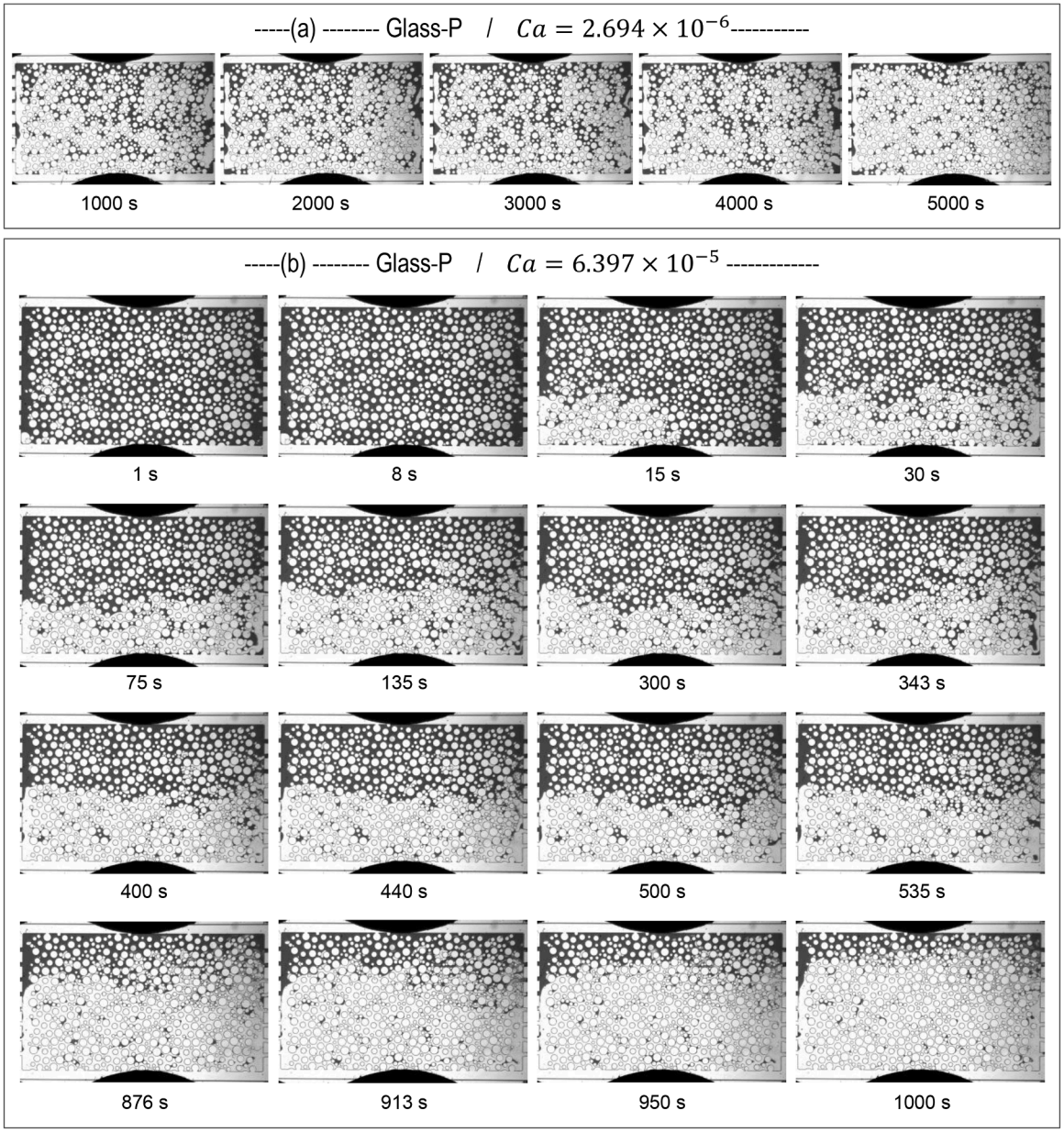


Fig. 6. Selected snapshots from steady-state co-injections, Glass-P network. WP is black, NWP is transparent. Flow direction is from left to right. Numbers indicate time lapse from injection start. (a) $\boldsymbol{Ca} = 2.694 \times 10^{-6}$ (1000–5000 s) (b) $\boldsymbol{Ca} = 6.397 \times 10^{-5}$ (1-1000 s).

and the plateau phase (flattening-out) of the sigmoid curves delineating the maximum values of the energy efficiency of the process (Section 4.2). A similar trend can be observed between the successive increments in the flow-rate ratio for every constant-*Ca* experiment. Albeit spanning over different regions in the *Ca* domain, this decay trend is systematic for all the systems examined (PDMS-P, Glass-P and PDMS-NP). It is an indication of flow hysteresis associated with geometrical/topological reconfiguration of the flow structure of the disconnected NWP until a local energy minimum is reached (Cueto-Felgueroso and Juanes, 2016; Rücker et al., 2021).

Indicative snapshots of the interstitial flow structure evolution are presented in Fig. 6 for two co-injection experiments at $Ca = 2.694 \times 10^{-6}$ and $Ca = 6.397 \times 10^{-5}$ in the Glass-P model network. The WP (Deionized Water + Dye) is black, and the NWP (Fluorinert^{TM} FC-770) is transparent ("white").

The flow segregation observed in the snapshots in Fig. 6(b), pertains to WP injection at high *Ca* values. The fraction of segregation, between the WP (black) and NWP (transparent), increases with increasing flow-rate ratio. The snapshots on the 1st row in Fig. 6(b), record the initial moments of co-injection of the NWP with flow rate ratio $r = 1.7/9.5 = 0.18$; while those on the 2nd row indicate the flow structure during the successive flow-rate step-ups.

Flow segregation may be attributed to poor flow mixing downstream the two inlet ports as well as, self-structuring of the interstitial flow to adapt to the entry flow (initial) conditions. The latter is compatible with reduction of energy dissipation for the imposed flow conditions at high *Ca* and moderate to high *r* values. Flow mixing by disconnection of the NWP creates menisci, these increase pressure gradients and, consequently, energy dissipation increases. The flow segregation observed in the snapshots in Fig. 6(b), pertains to WP injection at high *Ca* values. The fraction of segregation, between the WP (black) and NWP (transparent), increases with increasing flow-rate ratio. The snapshots on the 1st row in Fig. 6(b), record the initial moments of co-injection of the NWP with flow rate ratio $r = 1.7/9.5 = 0.18$; while those on the 2nd row indicate the flow structure during the successive flow-rate step-ups. Flow segregation may be attributed to poor flow mixing downstream the two inlet ports as well as, self-structuring of the interstitial flow to adapt to the entry flow (initial) conditions. The latter is compatible with reduction of energy dissipation for the imposed flow conditions at high *Ca* and moderate to high *r* values. Flow mixing by disconnection of the NWP creates menisci, these increase pressure gradients and, consequently, energy dissipation increases.

In the same context, in an effort to correlate the evolution of the interstitial flow structure with the evolution of the pressures, we calculated the primary statistics (mean, cumulative mean, standard-deviation, skewness) and selected probabilities of the grayscale intensity for each recorded frame and for a variety of flow conditions at different networks. A typical time evolution of the aforementioned grayscale intensity primary statistics is presented in Fig. 7. The diagrams pertain to the flowrate ratio co-injections within the Glass-P model network at $Ca = 6.397 \times 10^{-5}$. In that figure, the time evolution of the measured pressures (top diagram) is exhibited against the evolution of primary statistics (middle diagram) and selected probabilities of the grayscale intensity (bottom diagram).

The above statistics show when in the timeline a steady-state has been reached for each flowrate bump-up under constant-*Ca*. The most significant index among the primary statistics seems to be the skewness coefficient (and the probability of grayscale intensity at 0.5, i.e. exactly between black and white color intensities), which is more sensitive compared to the mean and the standard-deviation for this type of experiment.

Please note, the present manuscript was intentionally limited to the basic image analysis, which was used to provide an overall indication of the evolution of the flow structure. A more detailed segmentation-based

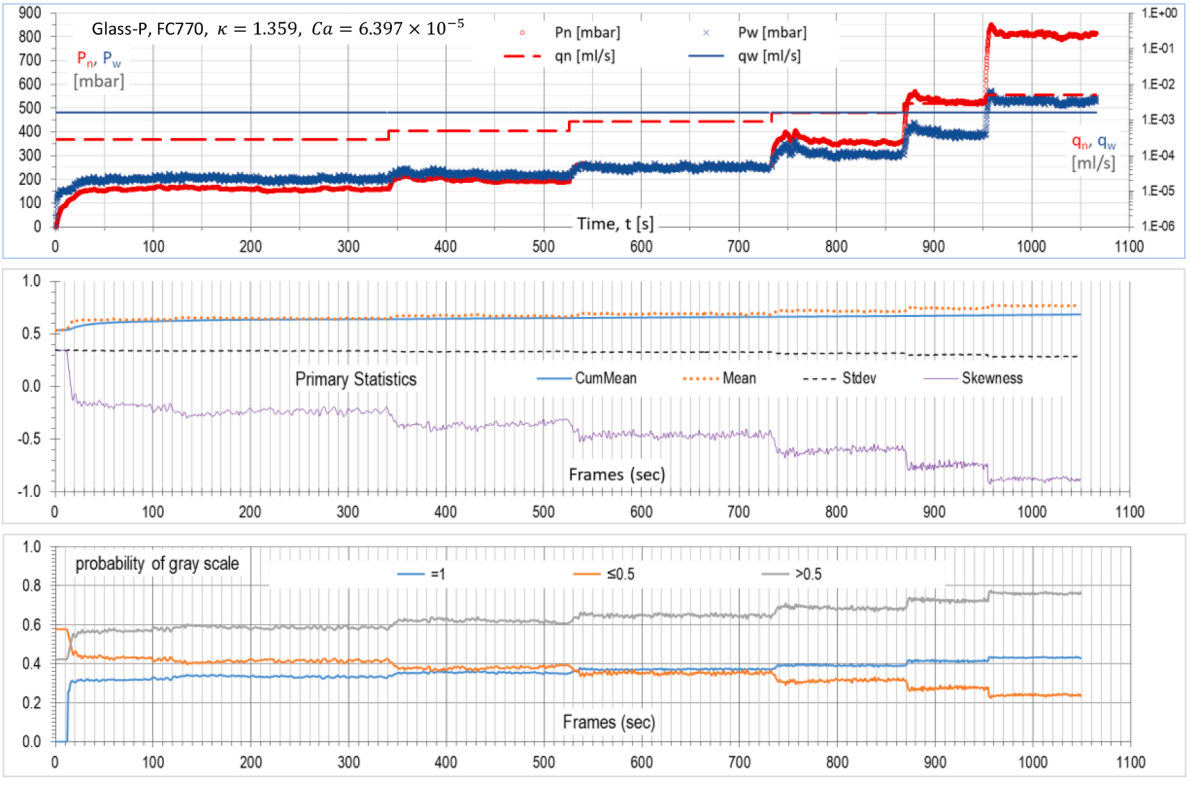


Fig. 7. Direct comparison of time evolution diagrams pertaining to the entire experiment of steady-state co-injection at $\boldsymbol{Ca} = 6.397 \times 10^{-5}$ in the Glass-P model network. Top – Pressure values measured at the inlet port, similar to diagrams presented in Fig. 5. Middle –Time evolution of the grayscale intensity primary statistics (mean, cumulative mean, standard-deviation, skewness) for each recorded frame pertaining to the entire network. Bottom – Selected probabilities of the grayscale intensity for each recorded frame.

analysis, including quantitative descriptors such as wetting-phase saturation, the size distribution of non-wetting-phase clusters, and their correlation with pressure fluctuations, dynamic capillary pressure, and energy efficiency, is the subject of a parallel study.

4. Results

The pair of pressure gradient values, $\{(\Delta\widetilde{p}/\Delta\widetilde{z})_n, (\Delta\widetilde{p}/\Delta\widetilde{z})_w\}$, was used to calculate the corresponding pair of relative permeability values for the NWP and WP, $\{k_{rn}, k_{rw}\}$, from Eq. (7). We need to stress here that we have considered the general condition that the flow may not be fully developed, therefore the NWP and WP pressure gradients would not be necessarily equal. In such general condition, $(\Delta\widetilde{p}/\Delta\widetilde{z})_n \neq (\Delta\widetilde{p}/\Delta\widetilde{z})_w$; therefore, the pairs of NWP and WP relative permeability values, $\{k_{rn}, k_{rw}\}$, were calculated using Eq. (15)

$$k_{rn} = \frac{\widetilde{\mu}_n \widetilde{U}_n}{\widetilde{k}\left(\frac{\Delta\widetilde{p}}{\Delta\widetilde{z}}\right)_n}, \quad k_{rw} = \frac{\widetilde{\mu}_w \widetilde{U}_w}{\widetilde{k}\left(\frac{\Delta\widetilde{p}}{\Delta\widetilde{z}}\right)_w} \tag{15}$$

The collected relative permeability values per constant-Ca experiment were plotted against the corresponding values of the flow-rate ratio, r, together with the corresponding values of energy efficiency, f_{EU}, Eq. (19), and mobility ratio, λ, Eq. (3). A total of 44 diagrams each per constant-Ca experiment are plotted. Due to space limitations a collection of representative diagrams spanning the entire region of constant-Ca experiments are presented in Fig. 8 for the PDMS-P network, and Figs. 9 and 10 for the Glass-P and PDMS-NP networks respectively.

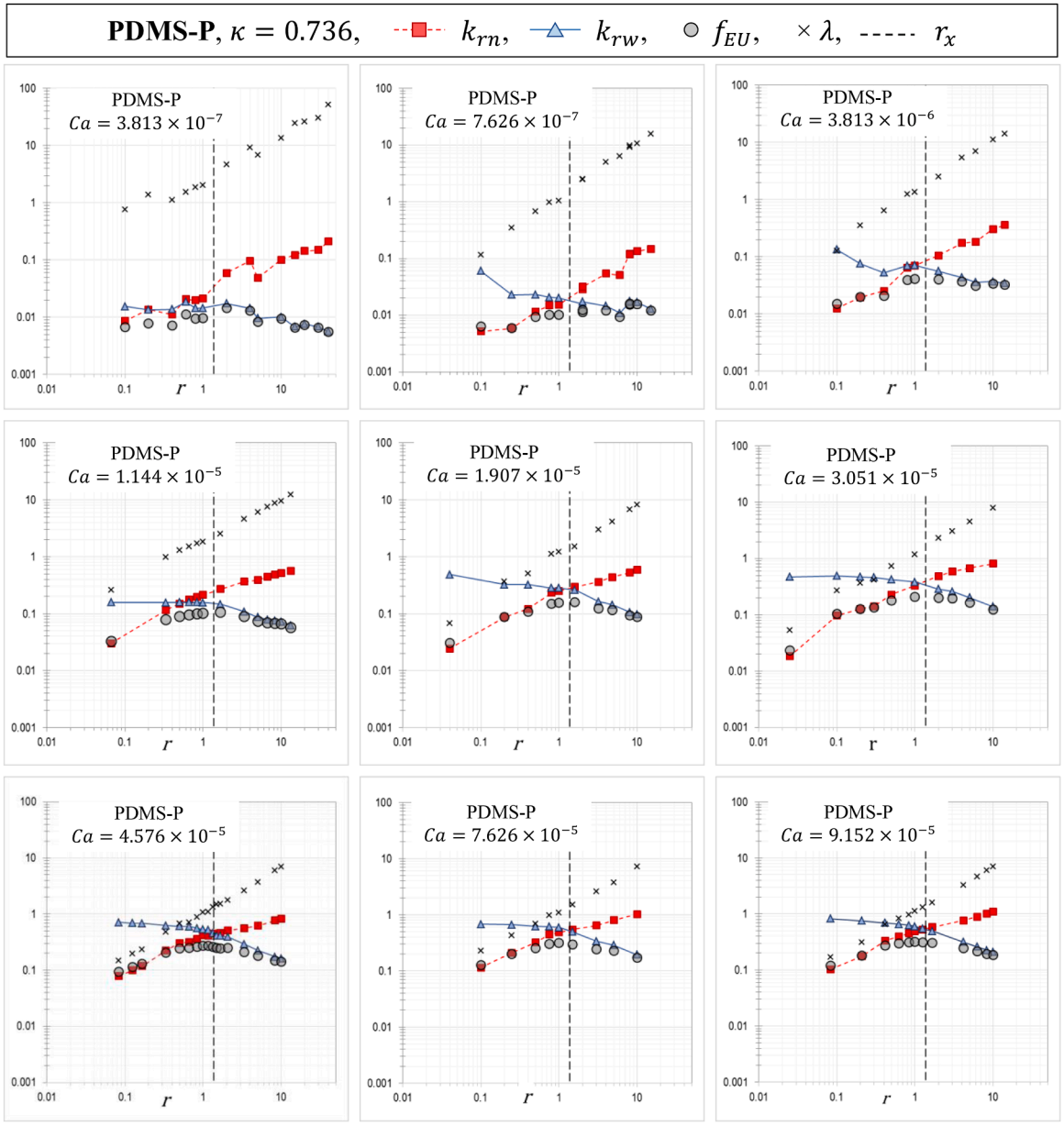


Fig. 8. Indicative diagrams of relative permeability for the NWP and WP (k_{rn},--■--, and k_{rw},—△—), energy efficiency, f_{EU} (●), and mobility ratio, λ (×) in terms of the flow-rate ratio, r. The diagrams pertain to the PDMS-P network. Each diagram corresponds to a constant- Ca experiment. The diagrams are arranged in order of increasing capillary number, Ca, progressing from left to right and from top to bottom. The vertical dashed lines denote the cross-over flow-rate ratios for relative permeability, as predicted by Eq. (11).

4.1. Relative permeability scaling incorporating flow-rate dependency logging and management

We proceed with revealing the flow dependent, relative permeability scaling for the steady-state two-phase co-injections in the three micro-fluidic pore networks.

Considering the flow is fully developed, we calculated the reduced pressure gradient, $x = 1/k_{rw}$, i.e. the inverse of the relative permeability of the WP using Eq. (8). The entire set of x values is plotted in terms of the flow-rate ratio, r, in the top-row diagrams and in terms of the capillary number, Ca, in the bottom-row diagrams in Fig. 11.

In particular, the values of reduced pressure gradient, x, are displayed in terms of log$r$, in groups of constant- Ca values. Note that with increasing r, there is an obviously systematic, asymptotic trend in aligning to the dashed, inclined line towards a virtually decoupled flow state. That is described by

$$\text{As } r\to\infty,\ \log x = \log\kappa + \log r \Leftrightarrow x = \kappa r \tag{16}$$

The inclination of the dashed line in the three log-log, top-row diagrams in Fig. 11, is equal to 1 : 1, and its pivot (marked by ○) is located at $\{1,\ \kappa\}$.

In the bottom-row diagrams in Fig. 11, the values of reduced pressure gradient, x, are displayed in terms of logCa, and lined-up in vertical rows of constant Ca. Within the same row, markers depict different values of the flow-rate ratio, r. As not all experiments were run on the same flow-rate ratio values, it is not possible to group the x-values into r-classes.

Again here, we may observe the tendency (a confluence) of the markers to converge and align – in an asymptotic manner – towards the inclined, dashed line (in red). The trend is described by

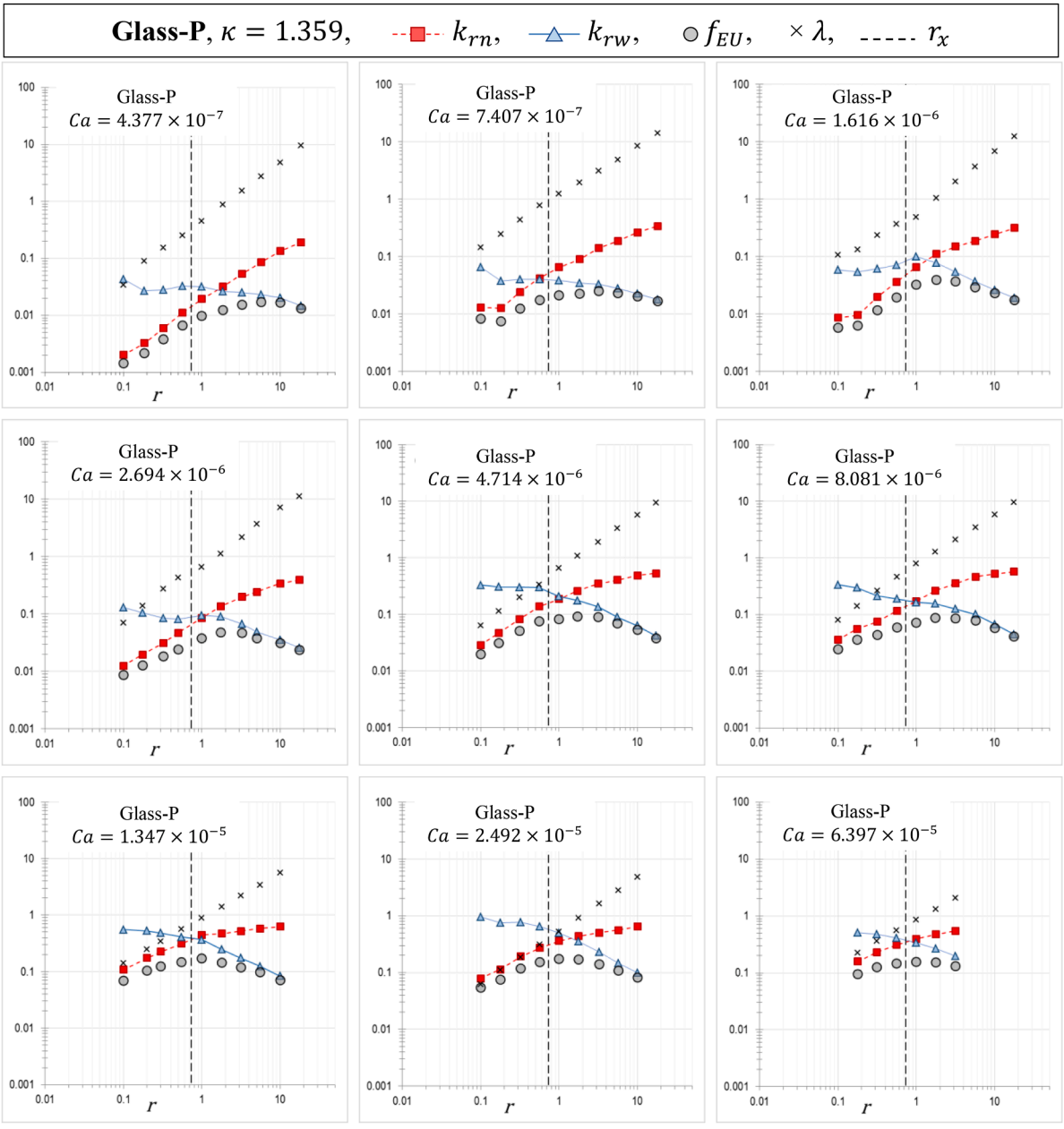


Fig. 9. Indicative diagrams of relative permeability for the NWP and WP (k_{rn},--■--, and k_{rw},—△—), energy efficiency, f_{EU} (○), and mobility ratio, λ (×) in terms of the flow-rate ratio, r. The diagrams pertain to the Glass-P network. Each diagram corresponds to a constant- Ca experiment. The diagrams are arranged in order of increasing capillary number, Ca, progressing from left to right and from top to bottom. The vertical dashed lines denote the cross-over flow-rate ratios for relative permeability, as predicted by Eq. (11).

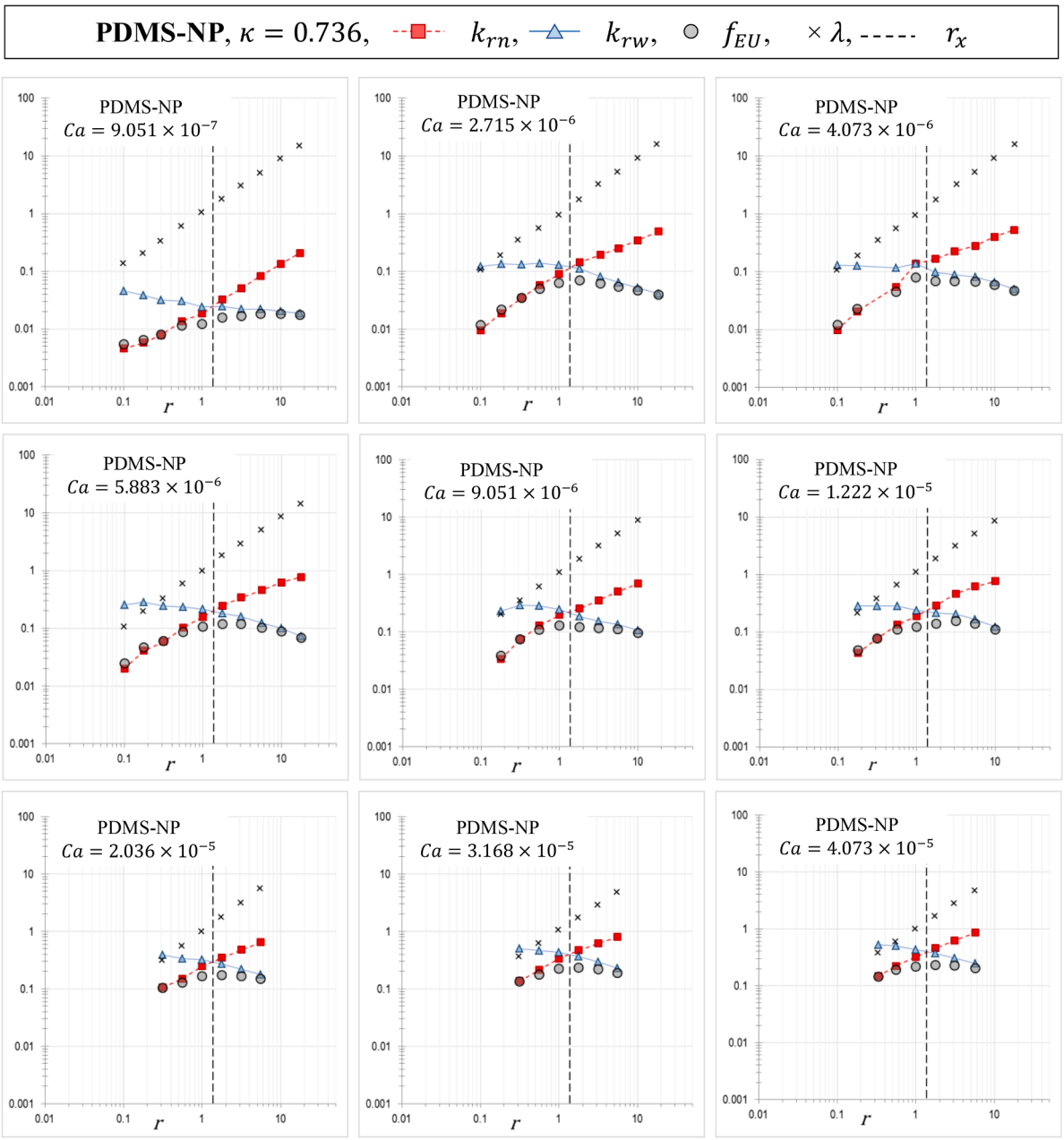


Fig. 10. Indicative diagrams of relative permeability for the NWP and WP (k_{rn},---■---, and k_{rw},—△—), energy efficiency, f_{EU} (●), and mobility ratio, λ (×) in terms of the flow-rate ratio, r. The diagrams pertain to the PDMS-NP network. Each diagram corresponds to a constant- Ca experiment. The diagrams are arranged in order of increasing capillary number, Ca, progressing from left to right and from top to bottom. The vertical dashed lines denote the cross-over flow-rate ratios for relative permeability, as predicted by Eq. (11).

$$\log Ca \ll 0,\ \log x = \log\kappa - \log C_{pm} - \log Ca \Leftrightarrow x = \kappa/(C_{pm}Ca) = Ca_{pm}/Ca \quad (17)$$

The functional form of this asymptote is given by an expression, up to a constant value, C_{pm}, associated to the NWP/WP/PM system (Valavanides, 2023). The line asymptote has a negative inclination with slope equal to −1. For the available set of data displayed in the bottom row diagrams, we have used arbitrary, best-guess, constant values $\log C_{pm}$, to pivot the line along the Ca axis at $Ca_{pm} = \kappa / C_{pm}$. The pivot is indicated by the thick red cross marker (+) in each diagram. By increasing these values but keeping the negative inclination equal to 1 : 1, the dashed lines (asymptotes) are transferred in parallel to the left, at lower Ca pivot points, and vice versa. The "best guess" values used to pivot the asymptotes in the diagrams do not have an effect on the following. To estimate the C_{pm} values more precisely, we need to have more data and, most importantly, the data should pertain to capillarity dominated flows, i.e. to flows at low Ca values, close to the confluence region of the data markers. The recovery of the correct C_{pm} value for a certain system is essentially a "dynamic network-typing" procedure. That is because the value of C_{pm} is associated to the interaction between the structure of the pore network and the wettability of the two-fluid system – the dynamic advancing and receding contact angles and the associated dynamic hysteresis.

The trend in the diagrams in Fig. 11 is similar to the trend observed in the *DeProF* model simulations (Valavanides, 2023) pertaining to a virtual sandstone network model. The same trend is observed in a similar diagram, pertaining to the lab study on a natural sandstone core (Valavanides et al., 2020). Recall that the inclined asymptotes describe or delineate the domain of flow conditions whereby the compound flow

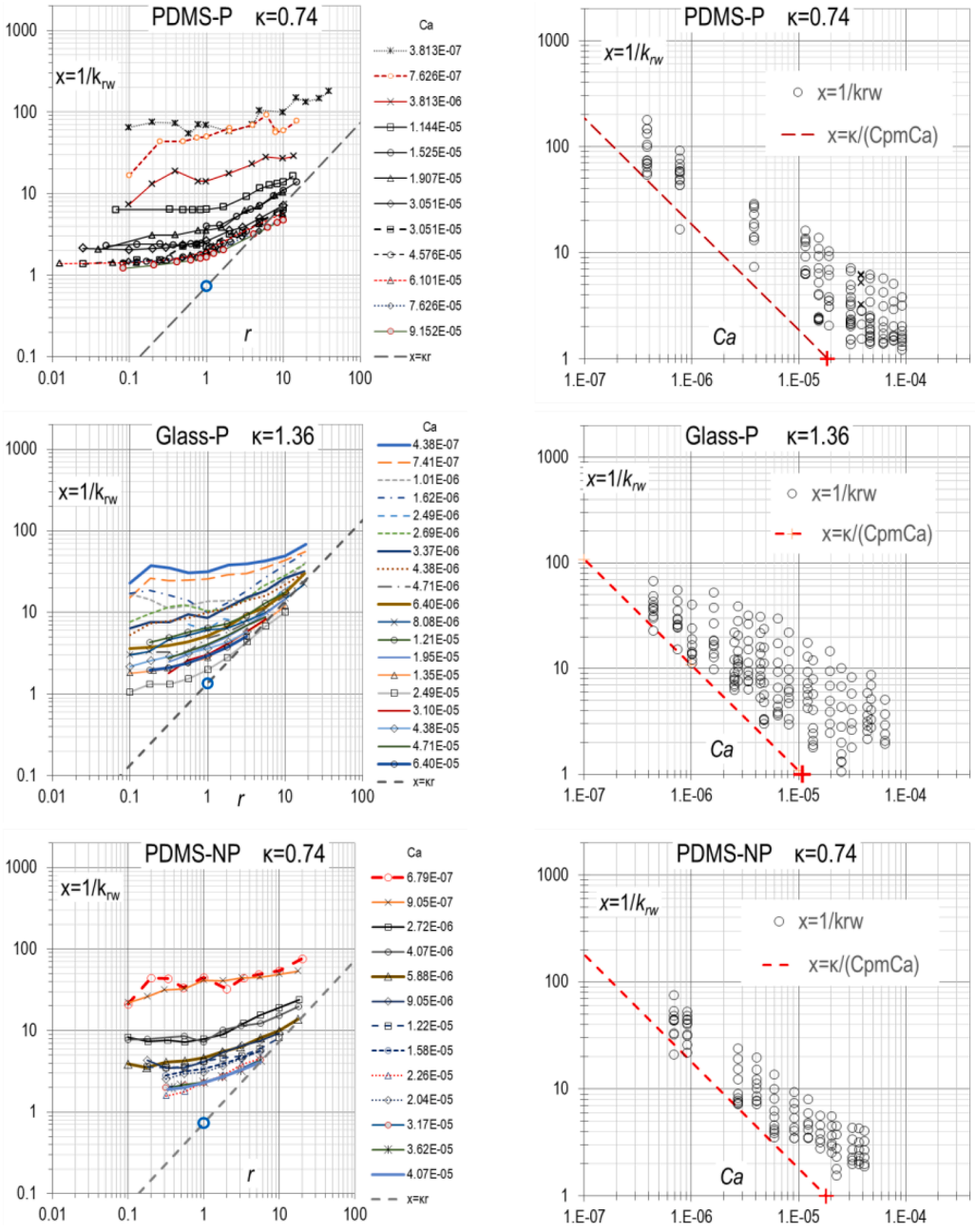


Fig. 11. Reduced pressure gradient (inverse WP relative permeability) values in terms of ***r*** for constant ***Ca*** values (left column), and reduced pressure gradient values in terms of ***Ca*** for different ***r*** values (right column), for the three NWP/WP/PM systems examined in the study (PDMS-P, top row, Glass-P, middle row and PDMS-NP, bottom row).

resistance, attributed entirely to the bulk phase viscosities, is partitioned on complementary volume fraction rations, namely, saturation. And it is only at those high flow-rate conditions (high-*Ca*) that relative permeabilities can be expressed in terms of saturation in a "saturation-dependency" fashion. Similar observations have been reported by Chevalier et al. (2015) albeit for the case of desaturation curves, i.e. when the WP is sweeping the NWP. A similar trend is observed in the very low-*Ca* regime (capillarity dominated flows); nevertheless that trend is a bit fuzzy as it depends strongly on the distribution of the menisci of the stranded ganglia within the network. That, on its turn, indicates history dependence.

In order to describe the steady-state two-phase flow in the particular microfluidic system, in the form of the universal scaling function Eq. (13), we need to reveal the associated kernel function, $A(\log Ca)$, namely the *Intrinsic Dynamic Capillary Pressure* (IDCP) curve (Valavanides, 2023). In essence, the IDCP represents the contribution of the capillary resistances within the overall flow resistance in any particular two-fluid and pore network flow system –hence the adjectives "intrinsic" and "dynamic". To reveal the IDCP for each examined system we have implemented the fitting procedure described in (Karadimitriou et al., 2023).

In the diagrams in Fig. 12, we plot the A_i values calculated in terms of Ca_i, via Eq. (13). The small black circles mark the IDCP values, A_{ij}, per r_j, aligned into rows of constant-Ca_i groups. Average values of $A_i = \langle A_{ij} \rangle$ per constant-Ca_i are marked with large red circles. These are fitted by a power law (red dashed curve),

$$\log A = aCa^{-b} \tag{18}$$

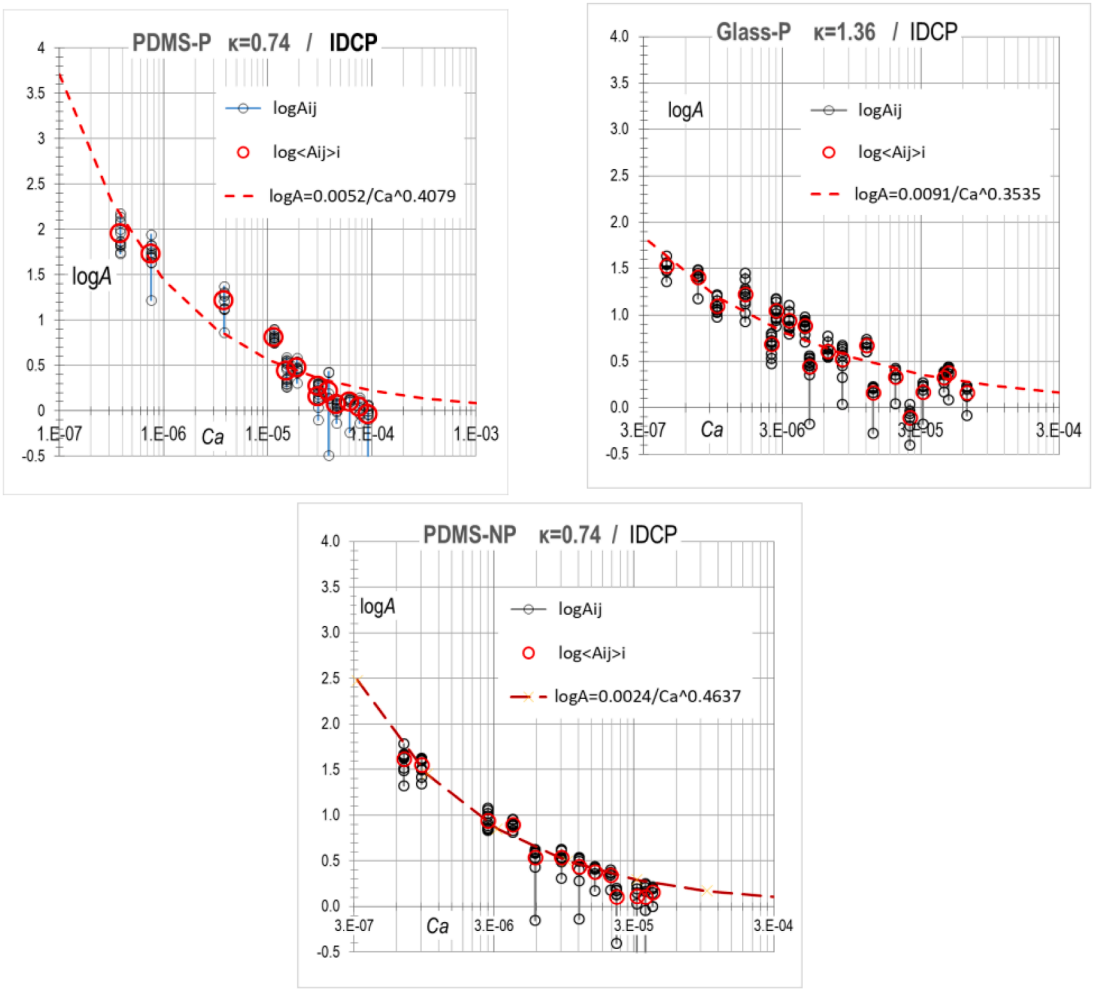


Fig. 12. Intrinsic dynamic capillary pressure function, $\boldsymbol{A}(\boldsymbol{Ca})$, Eq. (13), in terms of the capillary number $\boldsymbol{Ca}$.

The power law indicates that, asymptotically, as $Ca \to \infty$, $A(\log Ca)$ decays to 1, therefore Eq. (13) becomes $x \to 1 + \kappa r$, and the saturation dependency is recovered, yet in an asymptotic fashion, for the viscous flow regime. The values of the fitting coefficients a, b are exhibited in Table 3. Optionally, the standard deviations of the A_{ij}, values per constant-Ca_i, can be weighted-in to the square of errors to improve the power law fitting.

4.2. Energy efficiency & critical flow conditions

Energy efficiency analysis is a complementary method to reveal latent systematic trends and get a better image of the interstitial flow structure within the two-fluid/pore network systems examined in the study. Moreover, it can be used to identify characteristic differences in the three examined flow systems.

We have calculated the energy efficiency index values using the nominal expression, Eq. (12), but instead using the flow-rate ratio, we used the mobility ratio, λ, therefore,

Table 3
Power law fitting coefficients of the IDCP curve for the 3 two-fluid/network systems examined in the study.

Fitting coefficients, Eq. (18) $\log A = aCa^{-b}$	PDMS-P	Glass-P	PDMS-NP
a	0.0052	0.0091	0.0024
b	0.4079	0.3535	0.4637

$$f_{EU} = \frac{\lambda k_{rw}}{\lambda + 1} \tag{19}$$

In that context, the interstitial flow was described by the *kinetic*(Eq. (19)) rather than the *kinematic*(Eq. (12)) definition of the energy efficiency index.

The compound diagrams in Fig. 13 provide the results of the energy efficiency analysis, implementing Eq. (19), In particular, the diagrams in Fig. 13, display two sets of data.

Focusing on the lower part of the diagrams in Fig. 13, sets of small, light grey circles indicate the values of energy efficiency, $\left\{r_j, f_{EU,ij}\right\}$ per constant-Ca_i experiment (with reference to the collection of diagrams in Fig. 10).

For every constant-Ca_i experiment, a maximum value is detected from the energy efficiency values, $f_{EU,ij}$ as

$$f^*_{EU,i} = f^*_{EU}(Ca_i) = \max_j \left\{ f_{EU,ij}, Ca_i \right\} \tag{20}$$

These maximum values are marked by larger, dark grey circles. A remarkably smooth increase of the maximum energy efficiency values, f^*_{EU}, with increasing Ca, is observed. Moreover, depending on the flow conditions, the maximum energy efficiency of the process may increase by 2 orders of magnitude. Operation-wise, that is a quite important characteristic when designing this type of processes. The maximum values (filled circle markers) tend to reach a maximum value – the, so called, "ceiling of efficiency" (Valavanides, 2018(b)), that is given by

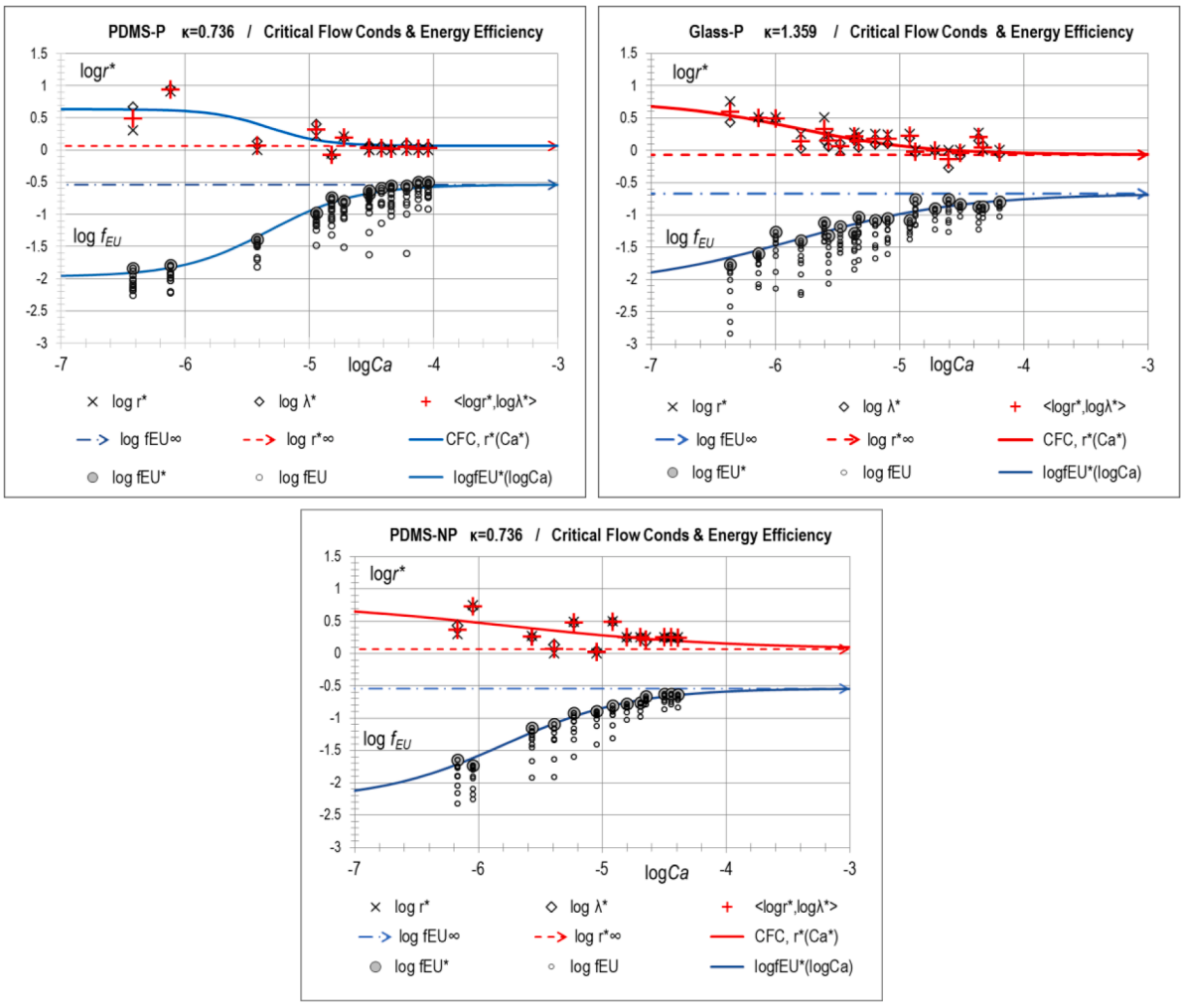


Fig. 13. Energy efficiency values $\{\boldsymbol{r}_j, \boldsymbol{f}_{EU,ij}\}$, ○, and detected maximum values $\{\boldsymbol{Ca}_i, \boldsymbol{f}^*_{EU,i}\}$, ●, for the three systems examined in the study (PDMS-P, Glass-P and PDMS-NP). The corresponding critical flow-rate ratio values, $\{\boldsymbol{Ca}_i, \boldsymbol{r}^*_i\}$, ×, and mobility ratio values, $\{\boldsymbol{Ca}_i, \boldsymbol{\lambda}^*_i\}$, ◇, define the so-called Critical Flow Conditions (CFC); upright cross markers in red, +, indicate the mean of the flow-rate ratio and mobility ratio values, $\widehat{\boldsymbol{r}}^*$, Eq. (23).

$$f^*_{EU\infty} = \left(1 + \sqrt{\kappa}\right)^{-2} \tag{21}$$

The f_{EU} values are marked on the logf_{EU} diagrams using small grey circles for the energy efficiency at different capillary number and flow-rate ratios $f_{EU}(Ca_i, r_j)$, and larger dark grey circles for the maximum values of energy efficiency at every capillary number, Ca_i.

The markers indicating the maximum efficiency values, $f^*_{\mathrm{EU}}(Ca_i)$, have been fitted by a 4 parameter sigmoid-curve, $f^*_{\mathrm{EU}}(Ca)$

$$\log f^*_{\mathrm{EU}}(Ca) = \log f^*_{\mathrm{EU}\infty} + \frac{\log f^*_{\mathrm{EU}0} - \log f^*_{\mathrm{EU}\infty}}{1 + exp[(\log Ca - \log Ca_m)/s_m]} \tag{22}$$

where:

$f^*_{\mathrm{EU}\infty}$ is the global maximum of the energy efficiency attained at the viscous (very high Ca) regime (the "ceiling" of the system's efficiency)

$f^*_{\mathrm{EU}0}$ is the energy efficiency at the capillary (very low Ca) regime,

These values delineate the two parallel asymptotic boundaries of the S-curve;

logCa_m is the logCa value for the $f^*_{\mathrm{EU}}(Ca)$ curve point that is midway between logr^*_0 and logr^*_∞;

s_m is the corresponding inclination of the curve.

The calculated values of the fitting parameters are presented in Table 4.

Refocusing on the upper part of the of the compound diagrams in Fig. 13, sets of markers indicate the critical flow conditions (CFCs), identified by observing the maximum values of the energy efficiency $f^*_{EU,i} = f^*_{EU}(Ca_i)$, Eq. (20), as evaluated by Eq. (19). Both critical flow-rate ratio, r^*_i, and mobility ratio, λ^*_i, are plotted in terms of logCa. A discrepancy between r^*_i and λ^*_i, is pronounced in the low-Ca domain, i.e. at capillarity-dominated flow regimes, while it is insignificant at the high-Ca domain where bulk viscosity prevails and the effect of menisci is practically negligible. The detected CFCs show a trend similar to a

Table 4
Characteristic parameter values for the three two-fluid/pore network systems examined in the study.

Parameter	PDMS-P	Glass-P	PDMS-NP
Maximum energy efficiency, $f^*_{EU}(Ca)$, Eq. (22)			
log$f^*_{EU\infty}$	−0.538	−0.671	−0.538
logf^*_{EU0}	−1.968	−2.100	−1.732
s_m	0.355	0.663	0.510
logCa_m	−5.325	−5.834	−5.790
Critical flow conditions, $r^*(Ca^*)$, Eq. (24)			
logr^*_∞	0.067	−0.067	0.067
logr^*_0	0.635	0.760	0.805
s_m	0.227	0.522	0.900
logCa_m	−5.325	−5.834	−5.790

sigmoid curve. As the trend is a bit fuzzy in the low-Ca regime, the log-averaged values were calculated as

$$\log\hat{r}^* = (\log r^* + \log\lambda^*)\Big/2 \Rightarrow \hat{r}^* = \sqrt{r^*\lambda^*} \tag{23}$$

These values are marked on the CFC diagrams using red, upright cross markers (+). Similarly to the energy efficiency maxima, the CFCs markers can be fitted by a 4 parameter sigmoid-curve

$$\log\hat{r}^* = \log r^*_\infty + \frac{\log r^*_0 - \log r^*_\infty}{1 + exp[(\log Ca - \log Ca_m)/s_m]} \tag{24}$$

where:

$\log r^*_\infty$ and r^*_0 are the critical flow-rate values at the viscous (very high Ca) and capillary (very low Ca) regimes respectively, and form the two parallel asymptotic boundaries of the S-curve;

$\log Ca_m$ is the $\log Ca$ value for the curve point that is midway between $\log r^*_0$ and $\log r^*_\infty$;

s_m is the corresponding inclination of the curve.

On the diagrams in Fig. 13, the dashed red, horizontal line indicates the nominal value of the critical flow-rate ratio for pure viscous flow conditions (as $Ca\to\infty$). Given the viscosity ratio of the two fluids, κ, the theoretical (nominal) value of the critical flow-rate ratio for pure viscous flow conditions (Valavanides 2018(a)) is estimated as

$$r^*_\infty = 1\Big/\sqrt{\kappa} \tag{25}$$

The actual value attained within the lower part of the sigmoid-curves, pertaining to larger Ca values, indicates an asymptotic trend, that is remarkably close to the theoretically predicted value, r^*_∞, Eq. (25). Moving on to the low-Ca regime (capillary flows) the observed fuzziness in locating the CFCs is attributed to significant capillary end effects.

The parameter values for the sigmoid-curves fitting the energy efficiency maxima and the CFCs, presented in Table 4, are estimated by minimizing the sum of the squared fitting errors. Comparing the sigmoid-curves for the CFCs in the two-fluid/pore network systems examined (ref. Fig. 13& Table 4) we observe that the transition from capillary to viscous flow is smoother (over a broader Ca region) in the PDMS-NP system ($s_m|_{Glass-P} < s_m|_{PDMS-NP}$) and the shift takes place at a larger Ca value ($\log Ca_m|_{Glass-P} < \log Ca_m|_{PDMS-NP}$). Overall, the trend across the three two-fluid/pore network systems examined is systematic. There are conceptual similarities to the diagrams furnished in the theoretical framework (Valavanides, 2018(b)), and also to the diagrams produced in the SCAL study by the IFP group (Valavanides et al., 2020) on a natural core (Clashach sandstone) across a broad domain of flow conditions.

4.3. Repeatability vs uncertainty

To investigate the repeatability of the measurements under various flow conditions we run replicate experiments. In addition to the conventional step-up procedure, in which the flow-rate ratio was progressively increased at each fixed capillary number, we also extended the co-injection at selected constant capillary numbers, by reverse, step-down decreases of the flow-rate ratio. This is described in a precursor work by Karadimitriou et al. (2023). The trends obtained from the two procedures (step-up, step-down in flowrate ratio) were similar, although the degree of repeatability depended on the flow regime.

In particular, we observed that repeatability was generally weaker in the low-capillary-number regime than at higher capillary numbers. This behavior is consistent with the expected influence of flow history in capillary-dominated two-phase flow. When capillary forces dominate over viscous forces, multiple stable interstitial flow configurations may be accessible, and the resulting flow structure can depend substantially on the preceding flow history. Conversely, at higher capillary numbers, viscous forces tend to reduce the persistence of such history-dependent configurations and the flow becomes more reproducible.

The influence of flow history was evaluated quantitatively through the Pearson correlation coefficient between values of the flowrate ratio and mobility ratio, for each constant-Ca experiment, as presented in Fig. 14. The results indicate that repeatability decreases, particularly at very low capillary numbers and low flow-rate ratios, where history dependence becomes more pronounced. This behavior is also related to the structure of the pore network, with substantial differences observed between periodic and non-periodic networks and viscosity ratio.

Regarding uncertainty quantification associated with the identification of the critical flow conditions, previous systematic SCAL analyses have shown that the confidence intervals associated with the critical-flow locus, $r^*(Ca)$, are comparatively narrow, indicating that the critical flow conditions and the associated maximum energy-efficiency conditions can be identified with relatively high confidence due to the structure of Eq. (10) and the trend of the relative peremabilities with the flowrate ratio (Valavanides et al., 2016).

Uncertainty should be interpreted in the context of the strong history dependence that characterizes the low-capillary-number regime. In such conditions, the observed variability is not necessarily only experimental noise; part of it reflects the intrinsic path dependence of the two-phase flow configuration.

4.4. Paradigms of application in SCAL

The relative permeability scaling model, which accounts for flow-rate dependency, together with the underlying theoretical framework proposed by Valavanides (2018, 2023)—including energy-efficiency analysis and critical flow conditions—warrants further validation using natural cores to assess its potential applicability in SCAL.

A central problem in SCAL is handling non-fully-developed flow conditions due to the presence of capillary end effects. Fully developed flow is not a condition always attained in SCAL measurements. The evolution of the interstitial flow, until fully developed flow conditions are reached downstream the entry ports, depends on the structure of the pore network, the wettability of the two-fluid/solid system and the superficial velocity of each fluid. In general, end effects are pronounced when capillarity-associated phenomena are not suppressed (overshadowed) by the prevailing viscous resistances.

Based on the findings of this preliminary study, the analysis presented here could be extended to SCAL experiments conducted on different types of natural cores. Analysis of ex-core measurements, combined with a series of calculations ranging from straightforward consistency checks (e.g., comparison of imposed flow-rate ratios with measured mobility ratios) to more advanced assessments, such as energy-efficiency analysis under varying flow conditions, can be used to identify the presence of end effects, quantify their magnitude, and characterize the pore network (network typing).

As a paradigm in assessing the degree to which the co-injected flows in the different networks have reached a fully-developed structure, we may focus on the diagrams in Fig. 10. Note that the markers (×) indicating values of the mobility ratio, λ_i, against, r_i, are – in general – aligned along a straight line with gradient 1:1. In many cases, the two values are practically equal, i.e. $\lambda_i = r_i$. For those cases, the kinetic states of the interstitial flow structures, λ_i, are consistent to the externally imposed, kinematic constraints, r_i, indicating that the corresponding flows are fully developed. Yet, in some diagrams pertaining to constant-Ca_i, we may observe some degree of discrepancy between the mobility ratio and the flow-rate ratio, manifested as a failure of the $\{\lambda_j, r_j\}|_{Ca_i}$ markers to perfectly align to the $r = \lambda$ straight line. That indicates these co-injections have not reached a fully-developed interstitial structure. We may evaluate the degree of misalignment and correlate it to the flow conditions and the two-fluid/network systems, by calculating the Pearson correlation coefficient between all sets of $\{\lambda_j, r_j\}|_{Ca_i}$ pairs per

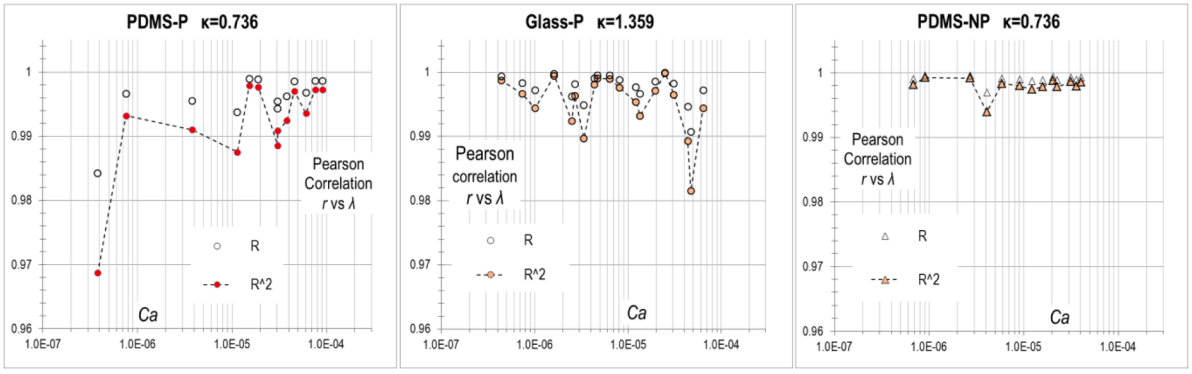


Fig. 14. Values of the Pearson correlation coefficient, R_i and ${R_i}^2$, between flow-rate ratio r_i and mobility ratio, λ_i for the entire set of experiments conducted at various Ca_i in the three model pore networks.

Ca_i. The results for all the constant-Ca experiments in the three systems are presented in Fig. 14.

We observe that the $\{\lambda_j, r_j\}|_{Ca_i}$ misalignment from linearity is pronounced in the two periodic networks (PDMS-P & Glass-P) when compared with that of the non-periodic (PDMS-NP), indicating significant presence of end effects in the periodic networks. The source of the $\{\lambda_j, r_j\}|_{Ca_i}$ misalignment may be attributed to the capillary end effects that are induced by the relatively stronger role of the menisci – when compared to the effects of the bulk viscosity. That may be attributed to the poorer interlacing of the two injected fluids upstream the network flow in the two periodic networks (PDM-P, Glass-P), compared to the single entry port of the PDMS-NP network – inciting a pre-mixing of the two fluids. We may also observe that the trends in the ${R_i}^2$, values vs Ca, for the PDMS-P and the Glass-P systems are reversed. That is an interesting behavior, especially considering that the viscosity ratio values are inverse ($\kappa = 1/1.36 = 0.74$ in the PDMS-P and $\kappa = 1.36$ in the Glass-P system). Moreover, albeit the two networks have the same plane geometry they have different 3D structures, i.e. orthogonal pores with smooth surface (PDMS-P), against pores with slightly irregular shape and micro-roughness respectively (Glass-P).

In the same context, in many diagrams in Fig. 10, pertaining to different constant-Ca experiments, the NWP and WP relative permeability curves intersect at the, so-called, relative permeability crossover flow-rate ratio value, $r_x = 1/\kappa$, Eq. (11), indicated by the vertical dashed line. Yet, in some constant-Ca experiments the relative permeability crossover does not coincide with the theoretical value of r_x and that is something also observed for the low, ${R_i}^2$, values, ref. Figs. 6 and 10, indicating an underlying trend.

Energy efficiency analysis provides another paradigm on characterizing the flow system, in compliance to the normative methodology proposed in (Valavanides, 2018(b)). Let us focus on the energy efficiency diagrams in Fig. 13 and, in particular, on the sigmoid curves interpolating the local maxima energy efficiency values $\left\{Ca_i, f^*_{EU,i}\right\}$. Based on these curves, for every two-fluid/network system, two nominal Ca values may be defined, corresponding to the apex of the two bends of the sigmoid curves. These bends segregate three distinct regions of the nominal Ca domain: the initial phase of the sigmoid curve, indicating low capillary flow conditions, the growth phase (sharp upward slope in the middle) indicating intermediate, capillary/viscous flow conditions, and the plateau phase (flattening-out) of the sigmoid curve indicating viscous flow conditions. This observation complies firmly with what we have observed (in Section 3.3) with respect to the trends of the magnitude of the pressure fluctuations, as well as the time delay and the minimization of the associated fluctuations in the three pressure evolution diagrams in Fig. 5.

These nominal values in Ca can be detected graphically or analytically, by setting the 2nd derivative of the expression (22), $\mathrm{d}^2\left(\log f^*_{\mathrm{EU}}\right)/\mathrm{d}Ca^2 = 0$ and solving for Ca. That of course comes at the extra cost of extensive measurements at various flow conditions to extract the maximum energy efficiency values and the CFCs. Yet, following the path of critical flow conditions will reduce the number of measurements. As discussed in (Valavanides et al., 2016) (ref. Fig. 3), if the co-injection conditions, (Ca, r), are maintained along the CFCs, uncertainties associated with measurement errors is minimized and specificity is maximized – that is mainly attributed to the structure of the f_{EU} expression, Eqs. (12) or (19). Therefore, tracking and aligning to the CFCs path during the SCAL measurements can provide more accurate /unbiased information per unit cost of measurements.

Please note, no sophisticated technology is needed to implement the proposed methodology. The measurements of pressure and flow-rates are conventional measurements taken outside the core (ex-core measurements).

Moreover, the same, ex-core measurements are used to reveal the IDCP curve, which essentially provides the backbone of the flow-rate dependency description, Eq. (13), of the two-fluid and core system. The form of the IDCP curve provides valuable information in assessing the extent of end effects and in deciphering the characteristics of the interstitial flow structure.

A convincing paradigm on how the IDCP curve may be used as a forensic tool in revealing the structure of the interstitial flow is provided in the systematic SCAL study performed by the IFP group on a core of natural Clashach sandstone (Valavanides et al., 2020). An analysis of the measured relative permeabilities, similar to that described in paragraph 4.1, revealed a sharply decreasing intrinsic dynamic capillary pressure function, $A(\log Ca)$, over moderate- to /high-Ca flow conditions. That seemed to be contradicting the smooth, asymptotic transition to zero $(\log A \to 0)$ depicted in Fig. 12 in the current study. Nevertheless the sharp decrease of A at moderate/high-Ca flow conditions was an indication of a sharp reduction of capillary resistances due to onset of emulsification.

In the current study, the trend in the IDCP functions, depicted in Fig. 12, shows asymptotic transitions to zero $(\log A \to 0)$ at the high-end of Ca. This is consistent to video observations of the interstitial flow structures comprising mixtures of connected WP and intermittent flows of disconnected NWP fluidic elements. The latter are separated from the WP through NWP/WP menisci remaining in contact to the pore walls. No signs of emulsification were observed.

In addition, the generalized specific characteristic invariants, pertaining to the two-fluid and pore network flow system, i.e. the locus of Critical Flow Conditions, the locus of cross-over relative permeability conditions, as well as the Intrinsic Dynamic Capillary Pressure curve, can be used as flow system identities and that could be a strong tool in developing flow system characterization ("rock-typing") methodologies and techniques.

In the reservoir engineering domain, the ability to handle a

functional form of the relative permeabilities, accounting for true-to-mechanism flow-rate dependency, through the IDCP curve, can definitely improve the specificity of field-scale simulators. That can be achieved by increasing the efficiency in physics-informed machine learning (PIML) interventions by integrating the physical laws into machine learning models to improve prediction accuracy, ensure physically plausible results, and reduce the need for massive data. The analysis based on energy efficiency could eventually provide a powerful tool in assessing the operational efficiency of enhanced oil recovery or CO_2 sequestration interventions, extending the energy transition timelines of such energy intensive activities.

Future research, should focus on the deployment of a similar study in natural cores.

CRediT authorship contribution statement

K.V. Mouravas: Visualization, Methodology, Investigation, Data curation. **N.K. Karadimitriou:** Writing – review & editing, Supervision, Resources, Methodology, Investigation, Data curation. **P.G. Dimitriadis:** Writing – review & editing, Visualization, Software. **A.G. Yiotis:** Writing – review & editing, Methodology. **H. Steeb:** Writing – review & editing, Supervision, Resources, Project administration, Funding acquisition. **M.S. Valavanides:** Writing – review & editing, Writing – original draft, Visualization, Supervision, Project administration, Investigation, Funding acquisition, Formal analysis, Data curation, Conceptualization.

Declaration of competing interest

I have nothing to declare.

Acknowledgements

M. Valavanides acknowledges support from the German Academic Exchange Service (DAAD-5752335 Research Stays for University Academics and Scientists, 2024) and from the Univ. of West Attica for his sabbatical leave.

K. Mouravas acknowledges support from Erasmus+ KA131 Placement mobility.

H. Steeb and N. Karadimitriou would like to thank the Deutsche Forschungsgemeinschaft (DFG, German Research Foundation) for supporting this work by funding SFB 1313, Project Number 327154368.

We gratefully acknowledge the reviewers for their constructive and insightful comments, which helped us improve the clarity, rigor, and overall quality of the original manuscript.

Data availability

The datasets containing the phase flowrates and the corresponding pressure drops, measured during the co-injection experiments in the three model pore networks, are available from the Data Repository of the University of Stuttgart (DaRUS) at doi:10.18419/DARUS-6561. For any clarifications or assistance, please contact the corresponding author.

References

Al-Sarihi, A., You, Z., Behr, A., Genolet, L., Kowollik, P., Zeinijahromi, A., Bedrikovetsky, P., 2020. Admissible parameters for two-phase coreflood and welge–JBN method. Transp. Porous Media 131, 831–871. https://doi.org/10.1007/s11242-019-01369-w.

Almutairi, A., Othman, F., Ge, J., Hussain, F., 2022. Modified Johnson–Bossler–Naumann method to incorporate capillary pressure boundary conditions in drainage relative permeability estimation. J. Pet. Sci. Eng. 210 (110064), 1–23. https://doi.org/10.1016/j.petrol.2021.110064.

An, S., Wenck, N., Manoorkar, S., Berg, S., Taberner, C., Pini, R., Krevor, S., 2023. Inverse modeling of core flood experiments for predictive models of sandstone and carbonate rocks. Water Resour. Res. 59 (e2023WR035526). https://doi.org/10.1029/2023WR035526.

Anastasiou, A., Zarikos, I., Yiotis, A., Talon, L., Salin, D., 2024. Steady-State dynamics of ganglia populations during immiscible two-phase flows in porous micromodels: effects of the capillary number and flow ratio on effective rheology and size distributions. Transp. Porous Media 151, 469–493. https://doi.org/10.1007/s11242-023-02041-0.

Andersen, P.Ø, 2021. Analytical modeling and correction of steady state relative permeability experiments with capillary end effects – an improved intercept method, scaling and general capillary numbers. Oil Gas Sci. Technol. – Rev. IFP Energ. Nouv. 76 (61), 61. https://doi.org/10.2516/ogst/2021045.

Andersen, P.Ø, Standnes, D.C., Skjæveland, S.M., 2017. Waterflooding oil-saturated core samples - analytical solutions for steady-state capillary end effects and correction of residual saturation. J. Pet. Sci. Eng. 157, 364–379. https://doi.org/10.1016/j.petrol.2017.07.027.

Andersen, P.O., Zhou, Y., 2020. Steady state relative permeability experiments with capillary end effects: analytical solutions including derivation of the intercept method. J. Pet. Sci. Eng. 192 (107249). https://doi.org/10.1016/j.petrol.2020.107249.

Andrew, M., Menke, H., Blunt, M.J., Bijeljic, B., 2015. The imaging of dynamic multiphase fluid flow using synchrotron-based X-ray microtomography at reservoir conditions. Transp. Porous Media 110, 1–24. https://doi.org/10.1007/s11242-015-0553-2.

API, American Petroleum Institute, 1998. Recommended Practice RP 40 "Recommended Practices for Core Analysis, 2nd Edition. 1998.

Armstrong, R.T., McClure, J.E., Berrill, M.A., Rücker, M., Schlüter, S., Berg, S., 2016. Beyond Darcy's law: the role of phase topology and ganglion dynamics for two-fluid flow. Phys. Rev. E 94, 043113. https://doi.org/10.1103/PhysRevE.94.043113.

Aursjo, O., Erpelding, M., Tallakstad, K.T., Flekkøy, E.G., Hansen, A., Maloy, K.J., 2014. Film flow dominated simultaneous flow of two viscous incompressible fluids through a porous medium. Front. Phys. 2 (63), 1–9. https://doi.org/10.3389/fphy.2014.00063.

Avraam, D.G., Kolonis, G.B., Roumeliotis, T.C., Constantinides, G.N., Payatakes, A.C., 1994. Steady-state two-phase flow through planar and nonplanar model porous media. Transp. Porous Media 16, 75–101. https://doi.org/10.1007/BF01059777.

Avraam, D.G., Payatakes, A.C., 1995. Flow regimes and relative permeabilities during steady-state two-phase flow in porous media. J. Fluid Mech. 293, 207–236. https://doi.org/10.1017/S0022112095001698.

Avraam, D.G., Payatakes, A.C., 1999. Flow mechanisms, relative permeabilities and coupling effects in steady-state two-phase flow in porous media. Case of strong wettability. Ind. Eng. Chem. Res. 38 (3), 778–786. https://doi.org/10.1021/ie980404o.

Bear, J., 2018. Modeling Phenomena of Flow and Transport in Porous Media, Theory and Applications of Transport in Porous Media. Springer. https://doi.org/10.1007/978-3-319-72826-1. ISBN: 978-3-319-72826-1 (eBook).

Berg, S., Ott, H., Klapp, S.A., Schwing, A., Neiteler, R., Brussee, N., Makurat, A., Leu, L., Enzmann, F., Schwarz, J.-O., Wolf, F., Kersten, M., Irvine, S., Stampanoni, M., 2013. Real-time 3D imaging of Haines jumps in porous media flow. Proc. Natl. Acad. Sci. 110 (10), 3755–3759. https://doi.org/10.1073/pnas.1221373110.

Berg, S., Unsal, E., Dijk, H., 2021. Sensitivity and uncertainty analysis for parameterization of multiphase flow models. Transp. Porous Media 140, 27–57. https://doi.org/10.1007/s11242-021-01576-4.

Berg, S., Armstrong, R.T., Rücker, M., Hansen, A., Kjelstrup, S., Bedeaux, D., 2026. From interface dynamics to Darcy scale description of multiphase flow in porous media. Adv. Colloid Interface Sci. 351 (103791), 1–65. https://doi.org/10.1016/j.cis.2026.103791.

Blunt, M.J., Jackson, M.D., Piri, M., Valvatne, P.H., 2002. Detailed physics, predictive capabilities and macroscopic consequences for pore-network models of multiphase flow. Adv. Water Resour. 25, 1069–1089. https://doi.org/10.1016/S0309-1708(02)00049-0kjj.

Borazjani, S., Hemmati, N., Behr, A., Genolet, L., Mahani, H., Zeinijahromi, A., Bedrikovetsky, P., 2021a. Determining water-oil relative permeability and capillary pressure from steady-state coreflood tests. J. Pet. Sci. Eng. 205, 108810. https://doi.org/10.1016/j.petrol.2021.108810.

Borazjani, S., Hemmati, N., Behr, A., Genolet, L., Mahani, H., Zeinijahromi, A., Bedrikovetsky, P., 2021b. Simultaneous determination of gas–water relative permeability and capillary pressure from steady-state corefloods. J. Hydrol. 598, 126355. https://doi.org/10.1016/j.jhydrol.2021.126355.

Brooks, R.H., Corey, A.T., 1964. Hydraulic properties of porous media. Hydrology Papers, No. 3. Colorado State University, Fort Collins, Colorado.

Buckley, S.E., Leverett, M.C., 1942. Mechanism of fluid displacement in sands. Trans. AIME 146 (01), 107–116. https://doi.org/10.2118/942107-G. SPE-942107-G.

Cao, J., James, L.A., Johansen, T.E., 2014. Determination of two phase flow relative permeability from core floods with constant pressure boundaries. In: SCA2014-074, *Intern. Symposium of the Society of Core Analysts*. Avignon, France, pp. 8–11. Sep.

Chen, A.L., Wood, A.C., 2001. Rate effects on water-oil relative permeability. In: SCA 2001-019, *Intern. Symposium of the Society of Core Analysts*. Scotland, Edinburgh, pp. 7–19. Sep.

Chevalier, T., Salin, D., Talon, L., Yiotis, A.G., 2015. History effects on nonwetting fluid residuals during desaturation flow through disordered porous media. Phys. Rev. E 91 (4), 043015. https://doi.org/10.1103/PhysRevE.91.043015.

Constantinides, G.N., Payatakes, A.C., 1989. A three dimensional network model for consolidated porous media. Basic studies. Chem. Eng. Commun. 81, 55–81. https://doi.org/10.1080/00986448908940530.

Constantinides, G.N., Payatakes, A.C., 2000. Effects of precursor wetting films in immiscible displacement through porous media. Transp. Porous Media 38, 291–317. https://doi.org/10.1023/A:1006557114996.

Cueto-Felgueroso, L., Juanes, R., 2016. A discrete-domain description of multiphase flow in porous media: rugged energy landscapes and the origin of hysteresis. Geophys. Res. Lett. 43, 1615–1622. https://doi.org/10.1002/2015GL067015.

Datta, S.S., Ramakrishnan, T.S., Weitz, D.A., 2014. Mobilization of a trapped non-wetting fluid from a three dimensional porous medium. Phys. Fluids 26 (022002). https://doi.org/10.1063/1.4866641.

Dell'Oca, A., Manzoni, A., Siena, M., Bona, N.G., Moghadasi, K., Miarelli, M., Renna, D., Guadagnini, A., 2023. Stochastic inverse modeling of transient laboratory-scale three-dimensional two-phase core flooding scenarios. Int. J. Heat Mass Transf. 202 (123716), 123716. https://doi.org/10.1016/j.ijheatmasstransfer.2022.123716.

Dullien, F.A.L., 1992. Porous media: fluid transport and pore structure, 2nd ed. Academic Press, San Diego. ISBN 978-0122236518.

Gao, Y., Lin, Q., Bijeljic, B., Blunt, M.J., 2020. Pore-scale dynamics and the multiphase Darcy law. Phys. Rev. Fluids 5, 013801. https://doi.org/10.1103/PhysRevFluids.5.013801.

Ge, J., Zhang, X., Liu, J., Almutairi, A., Hussain, F., 2022. Influence of capillary pressure boundary conditions and hysteresis on CO_2-water relative permeability. Fuel 321 (124132), 1–23. https://doi.org/10.1016/j.fuel.2022.124132.

Georgiadis, A., Berg, S., Makurat, A., Maitland, G., Ott, H., 2013. Pore-scale microcomputed-tomography imaging: nonwetting-phase cluster-size distribution during drainage and imbibitions. Phys. Rev. E 88 (033002), 1–9. https://doi.org/10.1103/PhysRevE.88.033002.

Goodarzian, S., Sorbie, K.S., 2023. Correct relative permeability data from steady-state experiments for capillary end effects. Geoenergy Sci. Eng. 224 (211626), 211626. https://doi.org/10.1016/j.geoen.2023.211626.

Grattoni, C.A., Bidner, M.S., 1990. History matching of unsteady-state corefloods for determining capillary pressure and relative permeabilities. In: SPE-21135-MS, SPE Latin America Petroleum Eng. Conf. Rio de Janeiro, Brazil. https://doi.org/10.2118/21135-MS. Oct 1990.

Gupta, R., Maloney, D.R., 2015. Applications of the intercept method to corrrect steady-State relative permeability for capillary end-effects. In: SCA2015-001, *Intern. Symposium of the Society of Core Analysts*. Canada, pp. 16–21. Aug.

Gupta, R., Maloney, D.R., 2016. Intercept method-A novel technique to correct steady-state relative permeability data for capillary end effects. SPE Res. Eval. Eng. 19, 316–330. https://doi.org/10.2118/171797-PA.

Hemmati, N., Borazjani, S., Badalyan, A., Genolet, L., Behr, A., Zeinijahromi, A., Bedrikovetsky, P., 2024. Determining relative permeability and capillary pressure from mixed-wet core floods. Geoenergy Sci. Eng. 239, 212885. https://doi.org/10.1016/j.geoen.2024.212885.

Huang, D.D., Honarpour, M.M., 1998. Capillary end effects in coreflood calculations. J. Pet. Sci. Eng. 19 (1–2), 103–117. https://doi.org/10.1016/S0920-4105(97)00040-5.

Johnson, E.F., Bossler, D.P., Naumann Bossler, V.O., 1959. Calculation of relative permeability from displacement experiments. In: Paper no SPE-1023-G *Trans*, 216, pp. 370–372. https://doi.org/10.2118/1023-G.

Kalule, R., Abderrahmane, H.A, Ahmed, S., Alameri, W., Al-Shalabi, E.W., 2026. Relative permeability and capillary pressure estimation via physics-informed machine learning and reinforcement learning. Petroleum 12 (3), 430–443. https://doi.org/10.1016/j.petlm.2026.04.005.

Karadimitriou, N., Valavanides, M.S., Mouravas, K., Steeb, H., 2023. Flow dependent relative permeability scaling for steady-state, two-phase flow in porous media: laboratory validation on a microfluidic network. Petrophysics 64 (5), 656–679. https://doi.org/10.30632/PJV64N5-2023a4.

Karadimitriou, N.K., Musterd, M., Kleingeld, P.J., Kreutzer, M.T., Hassanizadeh, S.M., Joekar-Niasar, V., 2013. On the fabrication of PDMS micromodels by rapid prototyping, and their use in two-phase flow studies. Water Resour. Res. 49 (4), 2056–2067. https://doi.org/10.1002/wrcr.20196.

Kerig, P.D., Watson, A.T., 1986. Relative-permeability estimation from displacement experiments: an error analysis. SPE-12589-PA. SPE Res. Eng. 1 (02), 175–182. https://doi.org/10.2118/12589-PA.

Lenormand, R., Lorentzen, K., Maas, J.G., Ruth, D., 2016. Comparison of four numerical simulators for SCAL experiments. In: SCA2016-006, *Intern. Symposium of the Society of Core Analysts*. Snowmass, Colorado, USA, 21-26 August 2016.

Leverett, M.C., 1941. Capillary behavior in porous solids. Trans. AIME 142, 152–169. 10.2118/941152-G.

Li, Y., Kang, Z., Liu, H., Kang, Z., Wei, Z., Jiang, L., Farouq Ali, S.M., Wang, S., 2025. A method to consider capillary end effect in relative permeability curves. J. Clean. Prod. 493 (144906), 144906. https://doi.org/10.1016/j.jclepro.2025.144906.

Maas, J.G., Schulte, A.M., 1997. Computer simulation of special core analysis flow experiments. In: SCA1997-19, Intern. Symposium of the Society of Core Analysts. Calgary, AB, Canada. https://scores-panterra.nl/Papers/SCA1997-19.pdf.

Maas, J.G., Springer, N., Hebing, A., 2019. Defining a sample heterogeneity cut-off value to obtain representative Special Core Analysis (SCAL) measurements. In: SCA 2019-024, *Intern. Symposium of the Society of Core Analysts*. Pau, France, Aug. 26-30. http://jgmaas.com/SCA/2019/SCA2019-024.pdf.

Masalmeh, S.K., Sorop, T., Suijkerbuijk, B.M.J.M., Vermolen, E.C.M., Douma, S., van del Linde, H.A., Pieterse, S.G.J., 2014. Low salinity flooding: experimental evaluation and numerical interpretation. IPTC-17558-MS. In: International Petroleum Technology Conference. Doha, Qatar, Jan. 2014. https://doi.org/10.2523/IPTC-17558-MS.

McPhee, C., Reed, J., Zubizarreta, I., 2015. Core Analysis, A Best Practice Guide. Elsevier. ISBN: 9780444636577.

Nguyen, V.H., Sheppard, A.P., Knackstedt, M.A., Pinczewski, W., 2006. The effect of displacement rate on imbibition relative permeability and residual saturation. J. Pet. Sci. Eng. 52, 54–70. https://doi.org/10.1016/j.petrol.2006.03.020.

Nono, F., Moonen, P., Berthet, H., Rivenq, R., 2019. Multiphase flow imaging through X-ray microtomography: reconsideration of capillary end-effects and boundary conditions. In: SCA2019-A081, *Intern. Symposium of the Society of Core Analysts*. Pau, France, Aug. 26–30, pp. 1–12.

Osoba, J.S., Richardson, J.G, Kerver, J.K., Hafford, J.A., Blair, P.M., 1951. Laboratory measurements of relative permeability. SPE-951047-G. J.Pet. Technol. 3 (02), 47–56. https://doi.org/10.2118/951047-G.

Oughanem, R., Youssef, S., Bauer, D., Peysson, Y., Maire, E., Vizika, O., 2015. A multi-scale investigation of pore structure impact on the mobilization of trapped oil by surfactant injection. Transp. Porous Media 109, 673–692. https://doi.org/10.1007/s11242-015-0542-5.

Pak, T., Butler, I.B., Geiger, S., Dijke, M.I.J., Sorbie, K.S., 2015. Droplet fragmentation: 3D imaging of a previously unidentified pore-scale process during multiphase flow in porous media. Proc. Natl. Acad. Sci. 112 (7), 1947–1952. https://doi.org/10.1073/pnas.1420202112.

Peksa, A.E., Wolf, K.H.A., Zitha, P.L.J., 2015. Bentheimer sandstone revisited for experimental purposes. Mar. Pet. Geol. 67, 701–719. https://doi.org/10.1016/j.marpetgeo.2015.06.001.

Rabinovich, A., Anto-Darkwah, E., Mishra, A.M., 2019. Determining characteristic relative permeability from coreflooding experiments: a simplified model approach. Water Resour. Res. 55 (11), 8666–8690. https://doi.org/10.1029/2019WR025156.

Rapoport, L.A., Leas, W.J., 1953. Properties of linear waterfloods. SPE 213-G. J. Pet Technol. 5 (05), 139–148. https://doi.org/10.2118/213-G.

Reed, J., Maas, J., 2018. Review of the intercept method for relative permeability correction using a variety of case study data. In: SCA2018-030, *Intern. Symposium of the Society of Core Analysts*. Trondheim, Norway, Aug. 26-31, pp. 1–14.

Reynolds, C.A., Menke, H., Andrew, M., Blunt, M.J., Krevor, S., 2017. Dynamic fluid connectivity during steady-state multiphase flow in a sandstone. Proc. Natl. Acad. Sci. 114 (31), 8187-81921-6. https://doi.org/10.1073/pnas.1702834114.

Richardson, J.G., Kerver, J.A., Hafford, J.A., Osoba, J.S., 1952. Laboratory determination of relative permeability. SPE-952187-G. J. Pet. Technol. 4 (08), 187–196. https://doi.org/10.2118/952187-G.

Rücker, M., Berg, S., Armstrong, R.T., Georgiadis, A., Ott, H., Schwing, A., Neiteler, R., N Brussee, N., Makurat, A., Leu, L., Wolf, M., Khan, F., Enzmann, F., Kersten, M., 2015. From connected pathway flow to ganglion dynamics. Geophys. Res. Lett. 42, 3888–3894. https://doi.org/10.1002/2015GL064007.

Rücker, M., Georgiadis, A., Armstrong, R.T., Ott, H., Brussee, N., van der Linde, H., Simon, L., Enzmann, F., Kersten, M., Berg, S., 2021. The origin of non-thermal fluctuations in multiphase flow in porous media. Front. Water 3 (671399), 1–25. https://doi.org/10.3389/frwa.2021.671399.

Ruth, D., 2020. Is contact angle a cause or an effect? – A cautionary tale. In: E3S Web of Conferences, 146. The International Symposium of the Society of Core Analysts, 03004. https://doi.org/10.1051/e3sconf/202014603004. SCA2019.

Sigmund, P.M., McCaffery, F.G., 1979. An improved unsteady-state procedure for determining the relative-permeability characteristics of heterogeneous porous media. SPE-6720-PA. SPE J. 19 (01), 15–28. https://doi.org/10.2118/6720-PA.

Singh, K., Bijeljic, B., Blunt, M.J., 2016. Imaging of oil layers, curvature and contact angle in a mixed-wet and a water-wet carbonate rock. Water Resour. Res. 52, 1716–1728. https://doi.org/10.1002/2015WR018072.

Sinha, S., Bender, A.T., Danczyk, M., Keepseagle, K., Prather, C.A., Bray, J.M., Thrane, L. W., Seymour, J.D., Codd, S.I., Hansen, A., 2017. Effective rheology of two-phase flow in three-dimensional porous media: experiment and simulation. Transp. Porous Media 119 (1), 77–94. https://doi.org/10.1007/s11242-017-0874-4.

Sinha, S., Gjennestad, M.A., Vassvik, M., Hansen, A., 2021. Fluid meniscus algorithms for dynamic pore-network modeling of immiscible two-phase flow in porous Media. Front. Phys. 8, 548497. https://doi.org/10.3389/fphy.2020.548497.

Spurin, C., Bultreys, T., Bijeljic, B., Blunt, M.J., 2019. Intermittent fluid connectivity during two-phase flow in a heterogeneous carbonate rock. Phys. Rev. E 100 (043103), 1–10. https://doi.org/10.1103/PhysRevE.100.043103.

Subbey, S., Christie, M., Sambridge, M., 2003. A strategy for rapid quantification of uncertainty in reservoir performance prediction. In: Paper presented at the SPE Reservoir Simulation Symposium, Houston, Texas, Feb. 2003. SPE Journal. 10.2118/79678-MS. Paper Number: SPE-79678-MS.

Tallakstad, K.T., Knudsen, H.A., Ramstad, T., Løvoll, G., Maløy, K.J., Toussaint, R., Flekkøy, E.G., 2009. Steady-state two-phase flow in porous media: statistics and transport properties. Phys. Rev. Lett. 102 (074502), 1–4. https://doi.org/10.1103/PhysRevLett.102.074502.

Tsakiroglou, C.D., Avraam, D.G., Payatakes, A.C., 2004. Simulation of the Immiscible Displacement in Porous Media Using Capillary Pressure and Relative Permeability Curves from Transient and Steady-State Experiments. International Symposium of the Society of Core Analysts, SCA2004-12, Abu Dhabi, UAE, 5-9 Oct 2004.

Tsakiroglou, C.D., Aggelopoulos, C.A., Terzi, K., Avraam, D.G., Valavanides, M.S., 2015. Steady-state two-phase relative permeability functions of porous media: a revisit. Int. J. Multiph. Flow 73, 34–42. https://doi.org/10.1016/j.ijmultiphaseflow.2015.03.001.

Valavanides, M.S., 2018a. Oil fragmentation, interfacial surface transport and flow structure maps for two-phase flow in model pore networks. Predictions based on extensive, DeProF model simulations. Oil Gas Sc. Technol. - Rev. IFP Energies Nouv. 73 (6), 6. https://doi.org/10.2516/ogst/2017033.

Valavanides, M.S., 2018b. Review of steady-state two-phase flow in porous media: independent variables, universal energy efficiency map, critical flow conditions, effective characterization of flow and pore network *transp*. Porous Media 123 (1), 45–99. https://doi.org/10.1007/S11242-018-1026-1.

Valavanides, M.S., 2023. Flow-rate dependency of steady-state two-phase flows in pore networks: universal, relative permeability scaling function and system characteristic

invariants. Transp. Porous Media 150, 521–557. https://doi.org/10.1007/s11242-023-02012-5.
Valavanides, M.S., Constantinides, G.C., Payatakes, A.C., 1998. Mechanistic model of steady-state two-phase flow in porous media based on ganglion dynamics. Transp. Porous Media 30, 267–299. https://doi.org/10.1023/A:1006558121674.
Valavanides, M.S., Daras, T., 2016. Definition and counting of configurational microstates in steady-state two-phase flows in pore networks. Entropy 18 (054), 54. https://doi.org/10.3390/e18020054.
Valavanides, M.S., Mascle, M., Youssef, S., Vizika, O., 2020. Steady-state two-phase flow in porous media: laboratory validation of flow dependent relative permeability scaling. In: E3S Web of Conferences, 146. The International Symposium of the Society of Core Analysts, 03002. https://doi.org/10.1051/e3sconf/202014603002. SCA2019.
Valavanides, M.S., Payatakes, A.C., 2001. True-to-mechanism model of steady-state two-phase flow in porous media, using decomposition into prototype flows. Adv. Water Resour. 24 (3–4), 385–407. https://doi.org/10.1016/S0309-1708(00)00063-4.
Valavanides, M.S., Totaj, E., Tsokopoulos, M., 2016. Energy efficiency characteristics in steady-state relative permeability diagrams of two-phase flow in porous media. J. Pet. Sci. Eng. 147, 181–201. https://doi.org/10.1016/j.petrol.2016.04.039.
Virnovsky, G.A., Skjaeveland, S.M., Surdal, J., Ingsoy, P., 1995. Steady-state relative permeability measurements corrected for capillary effects. SPE 30541. SPE ATCE, Dallas, Texas, pp. 22–25. https://doi.org/10.2118/30541-MS. Oct.
Wang, X., Li, S., Lv, P., Liang, C., Xu, J., Shi, M., Tong, B., Jiang, L., Liu, Y., Song, Y., 2025. Pore-scale intermittent flow and its impact on two-phase fluid distribution in porous media. Water Resour. Res. 61, e2025WR040858. https://doi.org/10.1029/2025WR040858.
Wegner, M.W., Christie, J.M., 1983. Chemical etching of deformation sub-structures in quartz. Phys Chem Miner. 9, 67–78. https://doi.org/10.1007/BF00308150.
Welge, H.J., 1952. A simplified method for computing oil recovery by gas or water drive. SPE-124-G. Trans. AIME 195, 91–98. https://doi.org/10.2118/124-G. *J Pet Technol* **4** (04), 91–98.
Wildenschild, D., Hopmans, J.W., Simunek, J., 2001. Flow rate dependence of soil hydraulic characteristics. Soil Sci. Soc. Am. J. 65, 35–48. https://doi.org/10.2136/sssaj2001.65135x.
Wildenschild, D., Sheppard, A.P., 2013. X-ray imaging and analysis techniques for quantifying pore-scale structure and processes in subsurface porous medium systems. Adv. Water Resour. 51, 217–246. https://doi.org/10.1016/j.advwatres.2012.07.018.
Wyckoff, R.D., Botset, H.G., 1936. The flow of gas-liquid mixtures through unconsolidated sands. Physics 7, 325–345. https://doi.org/10.1063/1.1745402.
Xia, Y., Whitesides, G.M., 1998. Soft lithography. Annu. Rev. Mater. Sci. 28, 153–184. https://doi.org/10.1146/annurev.matsci.28.1.153.
Yang, M., Liu, C., Li, Z., Li, Y., Du, D., 2026. Numerical evaluation of the pore structure effect-incorporated capillary number on the characterization of the immiscible two-phase displacement process in porous media. Chem. Eng. Sci. 331 (26), 124015. https://doi.org/10.1016/j.ces.2026.124015. PII:-X.
Yiotis, A.G., Dollari, A., Kainourgiakis, M.E., 2019. Nonlinear Darcy flow dynamics during ganglia stranding and mobilization in heterogeneous porous domains. Phys. Rev. Fluids 4, 114302. https://doi.org/10.1103/PhysRevFluids.4.114302.
Youssef, S., Mascle, M., Peysson, P., Vizika, O., 2017. CAL X: an X ray radiography tool for high throughput coreflood experimentation. Applications in the EOR context. SCA2017-012. Intern. Symp. Soc. Core Anal. 1–12. Vienna, Austria 28 Aug. - 1 Sept.
Youssef, S., Rosenberg, E., Deschamps, H., Oughanem, R., Maire, E., Mokso, R., 2014. Oil ganglia dynamics in natural porous media during surfactant flooding captured by ultra-fast x-ray microtomography. In: SCA 2014-023, *Intern. Symposium of the Society of Core Analysts*. France, pp. 1–12, 11-18 Sept.
Zhang, Y., Bijeljic, B., Gao, Y., Lin, Q., Blunt, M.J., 2021. Quantification of nonlinear multiphase flow in porous media. Geophys. Res. Lett. 48, e2020GL090477. https://doi.org/10.1029/2020GL090477.
Zhang, Y., Li, H., Yang, D., 2012. Simultaneous estimation of relative permeability and capillary pressure using ensemble-based history matching techniques. Transp. Porous Media 94, 259–276. https://doi.org/10.1007/s11242-012-0003-3.
Zou, S., Armstrong, R.T., Arns, J.-Y., Arns, C.H., Hussain, F., 2018. Experimental and theoretical evidence for increased ganglion dynamics during fractional flow in mixed-wet porous media. Water Resour. Res. 54, 3277–3289. https://doi.org/10.1029/2017WR022433.
Zou, S., Liu, Y., Cai, J., Armstrong, R.T., 2020. Influence of capillarity on relative permeability in fractional flows. Water Resour. Res. 56, e2020WR02762. https://doi.org/10.1029/2020WR027624.